Flower/FLWR-1 regulates neuronal activity *via* the plasma membrane Ca^{2+}-ATPase to promote recycling of synaptic vesicles

Marius Seidenthal[1,2], Jasmina Redzovic[1,2,3,4], Jana F. Liewald[1,2,4], Dennis Rentsch[1,2], Stepan Shapiguzov[1,2], Noah Schuh[1,2], Nils Rosenkranz[1,2], Stefan Eimer[3], Alexander Gottschalk[*,1,2]

1 Buchmann Institute for Molecular Life Sciences, Goethe-University, Max-von-Laue-Strasse 15, 60438 Frankfurt am Main, Germany
2 Institute for Biophysical Chemistry, Department of Biochemistry, Chemistry, and Pharmacy, Goethe-University, Max-von-Laue-Strasse 9, 60438 Frankfurt am Main, Germany
3 Institute of Cell Biology and Neuroscience, Goethe-University, Max-von-Laue-Strasse 13, 60438 Frankfurt am Main, Germany
4 Contributed equally
* to whom correspondence should be addressed: a.gottschalk@em.uni-frankfurt.de

Keywords: neurotransmission, synaptic vesicles, exo-endocytosis coupling, *Caenorhabditis elegans*, synaptic plasticity, excitation-inhibition imbalance, plasma membrane Ca^{2+}-ATPase

Abstract

The Flower protein was suggested to couple the fusion of synaptic vesicles (SVs) to their recycling in different model organisms. It is supposed to trigger activity-dependent bulk endocytosis by conducting Ca^{2+} at endocytic sites. However, this mode of action is debated. Here, we investigated the role of the *Caenorhabditis elegans* homolog FLWR-1 in neurotransmission. Our results confirm that FLWR-1 facilitates the recycling of SVs at the neuromuscular junction (NMJ). Ultrastructural analysis of synaptic boutons after hyperstimulation revealed an accumulation of large endocytic structures in *flwr-1* mutants. These findings do not support a role of FLWR-1 in the formation of bulk endosomes but rather a function in their breakdown. Unexpectedly, loss of FLWR-1 led to increased neuronal Ca^{2+} levels in axon terminals during stimulation, particularly in GABAergic motor neurons, causing excitation-inhibition imbalance. We found that this increased NMJ transmission might be caused by deregulation of MCA-3, the nematode orthologue of the plasma membrane Ca^{2+} ATPase (PMCA). *In vivo* molecular interactions indicated that FLWR-1 may be a positive regulator of the PMCA and might influence its recycling through modification of plasma membrane levels of $PI(4,5)P_2$.

Introduction

Chemical synaptic transmission involves a cycle of biogenesis of synaptic vesicles (SVs), their fusion with the plasma membrane (PM), as well as their recycling by endocytosis and de novo formation in the endosome (Alabi and Tsien, 2012; Chanaday et al., 2019; Kononenko and Haucke, 2015; Rizzoli, 2014; Saheki and De Camilli, 2012). Coupling of SV exocytosis and endocytosis must be tightly controlled to avoid depletion of the reserve pool of SVs and to enable sustained neurotransmission (Haucke et al., 2011; Lou, 2018). Different hypotheses have been formulated as to how this is achieved within neurons. One hypothesis suggests that an SV-integral transmembrane protein called Flower could form ion channels that get inserted into the PM during SV fusion (Yao et al., 2009). Subsequently, Flower may facilitate endocytosis by conducting Ca^{2+} into the cytoplasm, thus contributing to defining endocytic sites (Yao et al., 2017). In *Drosophila melanogaster*, Flower was proposed to increase phosphatidylinositol-4,5-bisphosphate ($PI(4,5)P_2$) levels through Ca^{2+} microdomains, which was suggested to drive activity-dependent bulk endocytosis (ADBE) and formation of new SVs after prolonged, intense neurotransmission (Li et al., 2020). The hypothesis that Flower may have Ca^{2+} channel activity was further proposed based on sequence similarities between Flower and the Ca^{2+} selectivity filter of voltage-gated Ca^{2+} channels (VGCCs; Yao et al. (2009). Additional evidence from *Drosophila* suggests that Flower may regulate clathrin-mediated endocytosis (CME) in a Ca^{2+} independent fashion (Yao et al., 2017). However, while a facilitatory role of Flower

in endocytosis appears to be evolutionarily conserved, and was observed in different organisms and tissues, including non-neuronal cells (Chang et al., 2018; Rudd et al., 2023; Yao et al., 2017), its Ca^{2+} channel activity and its influence on SV recycling is debated (Coelho and Moreno, 2020; Lou, 2018). The kinetics of Ca^{2+} rise mediated by Flower appear to be too slow and the amount conducted too low to have a major impact (Xue et al., 2012). Moreover, the function of Flower appears to depend on the cell type and the extent of synaptic activity (Chang et al., 2018; Yao et al., 2017). Apart from its role in endocytosis, Flower is involved in cell survival mechanisms during development (Coelho and Moreno, 2020; Costa-Rodrigues et al., 2021). Intriguingly, loss of the mammalian homolog of Flower can reduce tumor growth, suggesting an important function in tumor cell survival and indicating possible options for cancer treatment (Madan et al., 2019; Petrova et al., 2012). However, more research is needed to determine the exact signaling pathways by means of which Flower mediates cell survival (Costa-Rodrigues et al., 2021).

Early studies of the Flower protein proposed a two- or three-transmembrane helical organization in which the C-terminus is exposed to the extracellular space and may thus mediate intercellular communication (Costa-Rodrigues et al., 2021; Rhiner et al., 2010). However, more recent research has shown that both N- and C-termini of Flower are likely cytosolic, and that the longest mammalian isoform consists of four transmembrane helices which are connected by short loops (Chang et al., 2018; Rudd et al., 2023). The genome of the nematode *Caenorhabditis elegans* is predicted to contain only a single isoform of Flower (FLWR-1; *wormbase.org*). *C. elegans* therefore may serve as an excellent model organism to further investigate the evolutionarily conserved role of Flower in neurotransmission and endocytosis. Here, we studied the function of *C. elegans* FLWR-1. We find that FLWR-1 localizes to SVs and to the PM and is involved in neurotransmission. We further show that FLWR-1 has a facilitatory but not essential role in endocytosis, confirming previous research in *Drosophila* and mammalian cells. Loss of FLWR-1 surprisingly conveys increased Ca^{2+} levels in optogenetically depolarized motor neurons. Yet, this is accompanied by reduced neurotransmitter release based on pharmacological assays and following optogentic stimulation, thus suggesting a deregulation of Ca^{2+} signaling in the presynapse. This is associated with defective SV recycling at the level of the endosome and thus reduced SV numbers upon sustained stimulation. The increased Ca^{2+} level is more pronounced in γ-aminobutyric acid (GABA) releasing neurons and leads to an excitation-inhibition (E/I) imbalance at the neuromuscular junction (NMJ) through increased release of the neurotransmitter GABA. A function of FLWR-1 in endocytosis appears to affect also the plasma membrane Ca^{2+}-ATPase MCA-3, required for extrusion of Ca^{2+} from the cytosol. This may explain the increased Ca^{2+} levels during stimulation in *flwr-1* mutant neurons. Last, our findings suggest a possible direct molecular interaction between FLWR-1 and MCA-3.

Materials and methods

Molecular biology

For Plasmids used in this paper and details of their generation, see **Table S1**. **pZIM902** [punc-17b::GCaMP6fOpt] was a gift from Manuel Zimmer. **p1676** [punc-17(short)::TagRFP::ELKS-1] was kindly provided by the lab of Zhao-Wen Wang. **pJH2523** [punc-25::GCaMP3::UrSL2::wCherry] was a gift from Mei Zhen (Addgene plasmid # 191358 ; http://n2t.net/addgene:191358 ; RRID:Addgene_191358) (Lu et al., 2022).

Cultivation of *C. elegans*

Animals were kept at 20 °C on nematode growth medium (NGM) plates seeded with OP50-1 bacteria (Brenner, 1974). For optogenetic experiments, OP50-1 was supplemented with 200 µM all-*trans* retinal (ATR) prior to seeding and animals were kept in darkness. Transgenic animals carrying extrachromosomal arrays were generated by microinjection into the gonads (Fire, 1986). L4 staged larvae were picked ~18 h before experiments and tested on at least three separate days with

animals picked from different populations. Transgenic animals were selected by fluorescent markers using a Leica MZ16F dissection stereo microscope. Integration of the *sybIs8965* transgenic array (PHX8965 strain) was performed by SunyBiotech. The RB2305 strain containing the *flwr-1(ok3128)* allele was outcrossed three times to N2 wild type. For an overview of strains, genotypes and transgenes, see **Table S2**.

Counting live progeny

To count living progeny per animal, five L4 larvae were singled onto NGM plates seeded with 50 µl OP50-1. Animals were then picked onto fresh plates after two days and on each of the following two days and removed on day five. Living progeny per animal were counted after reaching adulthood and summed up over the three plates on which each parental animal laid eggs, respectively. Experiments were performed blinded to the genotype.

Pharmacological assays

1.5 mM aldicarb and 0.25 mM levamisole plates were prepared by adding the compounds to liquid NGM prior to plate pouring (Mahoney et al., 2006). Aldicarb (Sigma Aldrich, USA) was kept as a 100 mM stock solution in 70 % ethanol. Levamisole (Sigma Aldrich, USA) was stored as a 200 mM solution dissolved in ddH_2O. 12 - 30 young adult animals were transferred to each plate and tested every 15 (levamisole) or 30 (aldicarb) minutes. Assays were performed blinded to the genotype and control groups (wild type and *flwr-1* mutants), measured in parallel on the same day. Animals that did not respond after being prodded three times with a hair pick were counted as paralyzed. Worms that crawled of the plate were disregarded from analysis.

Measurement of swimming cycles and crawling speed using the multi-worm-tracker (MWT)

Swimming cycles were measured as described previously (Vettkotter et al., 2022). In short, worms were washed three times with M9 buffer to remove OP50 and transferred onto 3.5 cm NGM plates with 800 µl M9. Animals were visualized using the multiworm tracker (MWT) platform (Swierczek et al., 2011) equipped with a Falcon 4M30 camera (DALSA). Channelrhodopsin-2 (ChR2) was stimulated with 470 nm light at 1 mW/mm^2 intensity for 90 s. 30 s videos were captured and thrashing was analyzed using the "wrmTrck" plugin for ImageJ (Nussbaum-Krammer et al., 2015). The automatically generated tracks were validated using a custom written Python script (https://github.com/dvettkoe/SwimmingTracksProcessing). Crawling speed was measured with the same setup and as described before (Vettkotter et al., 2022) yet animals were transferred to empty, unseeded NGM plates after washing. Prior to the measurement, animals were incubated in darkness for 15 min which is necessary for a switch from local to global search for food and thus a constant crawling speed (Calhoun et al., 2014). The crawling speed was recorded with the "Multi-Worm Tracker" software and extracted using the "Choreography" software (Swierczek et al., 2011). A custom-written Python script was used to summarize the measured tracks (https://github.com/dvettkoe/MWT_Analysis).

For manual counting of swimming cycles (**Figure 9 – Figure supplement 1**), animals were transferred on an NGM plate in M9 buffer, and filmed with a Canon Powershot G11 camera, for 30 sec. Swimming cycles were counted manually during replay of the video.

Measurement of body length

Body length was measured as described previously (Liewald et al., 2008; Seidenthal et al., 2022). In short, single animals were transferred onto unseeded NGM plates and illuminated with light from a 50 W HBO lamp which was filtered with a 450 - 490 nm bandpass excitation filter. ChR2 was stimulated with 100 $\mu W/mm^2$ light intensity. A 665 - 715 nm filter was used to avoid unwanted activation by brightfield light. Body length was analyzed using the "WormRuler" software (version 1.3.0) and normalized for the average skeleton length before stimulation (Seidenthal et al., 2022). Values deviating more than 20 % from the initial body length were discarded as they result from artifacts in the background correction (and are biomechanically impossible). Basal body length was calculated from the skeleton length in pixels which is generated by the WormRuler software. This was converted to mm and averaged for each animal over a duration of five seconds.

Light microscopy and fluorescence quantification

Animals were placed upon 7 % agarose pads in M9 buffer. Worms were immobilized by either using 20 mM levamisole in M9 or Polybead polystyrene microspheres (Polysciences) for experiments involving GABAergic stimulation. For optogenetic experiments, single animals were placed upon pads to avoid unwanted pre-activation of channelrhodopsins. Imaging was performed using a Axio Observer Z1 microscope (Zeiss, Germany). Proteins were excited using 460 nm and

590 nm LEDs (Lumen 100, Prior Scientific, UK) coupled via a beamsplitter. Background correction was conducted by placing a region of interest (ROI) within the animal yet avoiding autofluorescence.

GCaMP and pHluorin imaging and ChrimsonSA stimulation was performed using a 605 nm beamsplitter (AHF Analysentechnik, Germany) which was combined with a double band pass filter (460 - 500 and 570 - 600 nm). A single bandpass emission filter was used (502.5 - 537.5 nm). pOpsicle assays were performed as described previously using a 100x objective (Seidenthal et al., 2023). We extended the ChrimsonSA stimulation light pulse to 30 s to be consistent with the stimulus length of electron microscopy (EM) and electrophysiology experiments. Moreover, 2 x 2 binning was applied. Image sequences with 200 ms light exposure (5 frames per second) were acquired with an sCMOS camera (Kinetix 22, Teledyne Photometrics, USA). Video acquisition was controlled using the µManager v.1.4.22 software (Edelstein et al., 2014). The timing of LED activation was managed using a *Autohotkey* script. Dorsal nerve cord (DNC) fluorescence was quantified with ImageJ by placing a ROI with the *Segmented Line* tool. XY-drift was corrected using the *Template Matching* plugin if necessary. Animals showing excessive z-drift were discarded. A custom written python script was used to summarize background subtraction and normalization to the average fluorescence before pulse start (https://github.com/MariusSeidenthal/pHluorin_Imaging_Analysis).

GCaMP imaging was conducted similarly with the same setup and light intensity for ChrimsonSA stimulation (40 $\mu W/mm^2$) yet without binning. GCaMP fluorescence was quantified by placing ROIs around four synaptic puncta. Puncta fluorescence was averaged prior to background correction and normalization. Moreover, the bleach correction function of the python script was used which corrects fluorescence traces with strong bleaching. Strong bleaching is defined as the fluorescence intensity of the mean of the last second of measurement being less than 85% of the first second. The script performs linear regression analysis for DNC fluorescent traces and background ROI and corrects values prior to background correction. The increase in GCaMP fluorescence during stimulation was highly dependent on basal fluorescence values before stimulation and transient Ca^{2+} signals. This caused some measurements to show very strong increases in fluorescence. To avoid distortion of statistical analyses, we performed outlier detection for the increase during stimulation on all datasets with the Graphpad Prism 9.4.1 Iterative Grubb's method. The alpha value (false discovery rate) was set to 0.01.

For pOpsicle assays, animals were assessed for whether they exhibited a significant increase in fluorescence during stimulation, which was necessary for analysis of fluorescence decay after stimulation. A strong signal was determined as the maximum background corrected fluorescence during the light pulse (moving average of 5 frames) being larger than the average before stimulation plus 3x the standard deviation of the background corrected fluorescence before stimulation. Regression analysis of pHluorin fluorescence decay was performed as described previously by using Graphpad Prism 9.4.1 and fitting a "Plateau followed one-phase exponential decay" fit beginning with the first time point after stimulation to single measurements (Seidenthal et al., 2023). Animals that displayed no increase during stimulation as well as animals showing no decay or spontaneous signals after stimulation were discarded from analysis.

Comparison of dorsal and ventral (VNC) nerve cord fluorescence of GFP::FLWR-1 and mCherry::SNB-1 was conducted by imaging the posterior part of the animal where an abundance of synapses can be found. Images were acquired using the same beamsplitter and excitation filter as used for pOpsicle experiments but equipped with a 500 – 540 nm/600 – 665 nm double bandpass emission filter (AHF Analysentechnik, Germany) and 2 x 2 binning. The Arduino script "AOTFcontroller" was used to control synchronized 2-color illumination (Aoki et al., 2024). VNC and DNC fluorescence were analyzed by choosing single frames from acquired z-stacks in which nerve cords were well focused. Fluorescence intensities were quantified by placing a *Segmented Line* ROI. Kymographs were generated with the ImageJ *Multi Kymograph* function.

Confocal laser scanning microscopy was performed on a LSM 780 microscope (Zeiss, Germany) equipped with a Plan-Apochromat 63-x oil objective. The Zeiss Zen (blue edition) *Tile Scan* and *Z-Stack* functions were used to generate overview images of animals expressing GFP::FLWR-1. Images were processed and maximum z-projection performed using ImageJ. Colocalization analysis was performed by placing a *Segmented Line* ROI onto the DNC and plotting the fluorescence profile along the selected ROI for both color channels. Correlation of fluorescence intensities was then conducted using the GraphPad Prism 9.4.1 Pearson correlation function.

Fluorescence of GFP within coelomocytes (CCs) was visualized with a 100-x objective. An eGFP filter cube (AHF Analysentechnik, Germany) was used and fluorescence was excited with the 460 nm LED. Images were acquired using 2 x 2 binning and 50 ms exposure for ssGFP and 200 ms for GFP fused to the PH-domain. Endocytosed ssGFP fluorescence was quantified by drawing a ROI around all CCs found within any worm imaged using the *Freehand selections* tool and performing background correction. CC fluorescence was then normalized to the average fluorescence in wild type animals on the respective measurement day and CC location (anterior/middle/posterior). This was necessary since anterior CCs

generally had a higher fluorescence than those in other locations. Membrane localization of PH-domain GFP was determined by drawing a *Segmented Line* ROI around the perimeter of the cell and drawing a rough outline of the cell interior using the *Freehand selections* tool. Membrane fluorescence was then corrected by subtracting the measured interior fluorescence for each cell.

In BiFC experiments, split mVenus was imaged with a 100x objective, the eGFP filter cube and 500 ms exposure. Fluorescence was excited with 460 nm.

MCA-3b::YFP was imaged with a 40-x objective, the eGFP filter cube and 200 ms exposure. Fluorescence was excited with 460 nm. Synaptic puncta towards the posterior part of the animal were imaged and quantified by drawing a *Freehand selections* ROI around all visible and well-focused synaptic puncta in an animal before averaging. Similarly, interpuncta fluorescence was quantified by drawing a ROI around several locations inbetween the examined puncta.

Primary neuronal cell culture

Primary neuronal cell cultures were generated from embryos of SNG-1::pHluorin expressing animals as described before (Seidenthal et al., 2023) yet seeded into perfusion chambers (0.4 mm channel height, ibidi). pHluorin fluorescence was excited with 460 nm and imaged using the eGFP filter cube and 1000 ms exposure time. The buffers used to quench surface and dequench intracellular pHluorin were adapted from Dittman and Kaplan (2006). Cells were washed three times with the respective buffer prior to imaging by pipetting 1 ml into the reservoir wells of the perfusion chamber and removing the same amount of liquid from the other side. Individual cells were analyzed by placing a *Segmented Line* ROI onto extending neurites and performing background correction. The fraction of SNG-1::pHluorin which resides in SVs was then estimated by dividing the fluorescence originating from vesicular pHluorin by the total fluorescence originating in unquenched pHluorin:

$$Vesicle\ fraction = \frac{F_{NH4Cl} - F_0}{F_{NH4Cl} - F_{pH=5.6}}$$

F_0 → the basal neurite fluorescence in control saline buffer

F_{NH4Cl} → neurite fluorescence during addition of a buffer containing NH_4Cl which unquenches intravesicular pHluorin

$F_{pH=5.6}$ → neurite fluorescence with surface quenched pHluorin by low pH

Electrophysiology

Electrophysiological recordings of body wall muscle cells (BWMs) were performed in dissected adult worms as previously described (Liewald et al., 2008). Animals were immobilized with Histoacryl L glue (B. Braun Surgical, Spain) and a lateral incision was made to access NMJs along the anterior VNC. The basement membrane overlying BWMs was enzymatically removed by 0.5 mg/ml collagenase for 10 s (C5138, Sigma-Aldrich, Germany). Integrity of BWMs and nerve cord was visually examined via DIC microscopy.

Recordings from BWMs were acquired in whole-cell patch-clamp mode at 20-22 °C using an EPC-10 amplifier equipped with Patchmaster software (HEKA, Germany). The head stage was connected to a standard HEKA pipette holder for fire-polished borosilicate pipettes (1B100F-4, Worcester Polytechnic Institute, USA) of 4–10 MΩ resistance. The extracellular bath solution consisted of 150 mM NaCl, 5 mM KCl, 5 mM $CaCl_2$,1 mM $MgCl_2$,10 mM glucose, 5 mM sucrose, and 15 mM HEPES, pH 7.3, with NaOH, ~330 mOsm. The internal/patch pipette solution consisted of 115 mM K-gluconate, 25 mM KCl, 0.1 mM $CaCl_2$, 5 mM $MgCl_2$, 1 mM BAPTA, 10 mM HEPES, 5 mM Na_2ATP, 0.5 mM Na_2GTP, 0.5 mM cAMP, and 0.5 mM cGMP, pH 7.2, with KOH, ~320 mOsm.

Voltage clamp experiments were conducted at a holding potential of −60 mV. Light activation was performed using an LED lamp (KSL-70, Rapp OptoElectronic, Hamburg, Germany; 470 nm, 8 mW/mm²) and controlled by the Patchmaster software. Subsequent analysis was performed using Patchmaster and Origin (Originlabs). Analysis of mPSCs was conducted with MiniAnalysis (Synaptosoft, Decatur, GA, USA, version 6.0.7) and rate and amplitude of mPSCs were analyzed in 1 s bins. Exponential decay of mPSCs during stimulation was calculated with Graphpad Prism 9.4.1 by fitting a one-phase exponential decay beginning with the first time point during stimulation.

232 **Transmission electron microscopy**

233 Prior to high-pressure freezing (HPF), L4 animals were transferred to freshly seeded *E. coli* OP50-1 dishes supplemented
234 with or without 0.1 mM ATR. HPF fixation was performed on young adult animals as described previously (Kittelmann et
235 al., 2013b; Weimer, 2006). Briefly, 20 - 40 animals were transferred into a 100 µm deep aluminum planchette (Microscopy
236 Services) filled with *E. coli* (supplemented with or without ATR, respectively), covered with a sapphire disk (0.16 mm)
237 and a spacer ring (0.4 mm; engineering office M. Wohlwend) for photostimulation. To prevent pre-activation of ChR2, all
238 preparations were carried out under red light. Animals were continuously illuminated for 30 s with a laser (470 nm, ~20
239 mW/mm²) followed 5 s later by HPF at -180 °C under 2100 bar pressure in an HPM100 (Leica Microsystems). Frozen
240 specimens were transferred under liquid nitrogen into a Reichert AFS machine (Leica Microsystems) for freeze substitution.

241 Samples were incubated with tannic acid (0.1% in dry acetone) fixative at -90 °C for 100 h. Afterward, a process of washing
242 was performed for substitution with acetone, followed by incubation of the samples in 2% OsO_4 (in dry acetone) for 39.5
243 h while the temperature was slowly increased up to room temperature. Subsequently, samples were embedded in epoxy
244 resin (Agar Scientific, AGAR 100 Premix kit – hard) by increasing epoxy resin concentrations from 50% to 90% at room
245 temperature and 100% at 60 °C for 48 h.

246 Electron micrographs of 2 – 5 individual animals, and from 12 – 22 synapses per treatment, were acquired by cutting cross
247 sections at a thickness of 40 nm, transferring cross sections to formvar- or pioloform covered copper slot grids. Specimens
248 were counterstained in 2.5% aqueous uranyl acetate for 4 min, followed by washing with distilled water, and incubation in
249 Reynolds lead citrate solution for 2 min in a CO_2-free chamber with subsequent washing steps in distilled water.

250 VNC regions were then imaged with a Zeiss 900 TEM, operated at 80 kV, with a Troendle 2K camera. Images were scored
251 and tagged blind in ImageJ (version 1.53c, National Institute of Health) as described previously, and analyzed using
252 SynapsEM (Vettkotter et al., 2022; Watanabe et al., 2020). Since the number of synaptic organelles varied between synapses
253 of different sizes, their counts were normalized to the average synaptic profile area of 145,253 nm^2. Large vesicles (LVs)
254 are defined by their size larger than 50 nm and empty lumen as described by (Kittelmann et al., 2013b), endosomes are
255 defined as structures larger than 100 nm and located more than 50 nm away from the dense projection, as described by
256 (Watanabe et al., 2014); however, by an alternative definition of endosome, structures with sizes larger than SVs and DCVs,
257 with an electron dense lumen were also included (Kittelmann et al., 2013b).

258 **Protein alignment and structure prediction**

259 Protein alignment was performed with ClustalX (Larkin et al., 2007) and shading of conserved residues created with
260 Boxshade (*https://junli.netlify.app/apps/boxshade/*). Transmembrane domains as well as membrane orientation were
261 predicted by entering the predicted amino acid sequence to DeepTMHMM (Hallgren et al., 2022). FLWR-1 structure was
262 modeled and visualized with Alphafold3 (AF3) (Abramson et al., 2024). FLWR-1 tetramers have been modeled using
263 AlphafoldMultimer or AF3 (Evans et al., 2022). Protein structures were analyzed and edited using PyMol v2.5.2. Docking
264 of $PI(4,5)P_2$ to the FLWR-1 AF3 model was conducted in PyMol using the DockingPie plugin running the Autodock/Vina
265 analysis (Eberhardt et al., 2021; Rosignoli and Paiardini, 2022).

266 **Statistical Analysis and generation of graphs**

267 Graphs were created and statistical analyses were performed using GraphPad Prism 9.4.1. Data was displayed as mean ±
268 standard error of the mean (SEM) unless noted otherwise. Unpaired t-tests were used to compare two datasets and one-way
269 ANOVAs or two-way ANOVAs if three or more datasets were assessed, according to the number of tested conditions.
270 Fitting of a mixed-effects model was used instead of two-way ANOVA if the number of data points was not constant
271 between different datasets for example if the number of animals differed between time points. Mann-Whitney tests were
272 performed if two datasets were compared that were not normally distributed and datasets were depicted as median with
273 interquartile range (IQR) in statistical analyses. Kruskal-Wallis tests were conducted if not normally distributed datasets
274 were assessed. Iterative Grubb's outlier detection was used when required and as indicated. The alpha value (false discovery
275 rate) was set to 0.01. Representations of the exon-intron structures of genes were created using the "Exon-Intron Graphic
276 Maker" (Bhatla, 2012).

277 # Results

278 ## FLWR-1 is involved in neurotransmission

279 The amino acid sequence of *C. elegans* FLWR-1 is conserved with its *D. melanogaster* (Fwe-
280 Ubi/FweA) and *Homo sapiens* (hFwe4) homologues (**Fig. 1A**). Fwe-Ubi/FweA was shown to facilitate
281 recovery of neurons, i.e. refilling of SV pools, following intense synaptic activity (Yao et al., 2009;
282 Yao et al., 2017). To investigate whether this involvement of Flower in neurotransmission is
283 evolutionarily conserved, we studied a mutant lacking most of the *flwr-1* coding region (*ok3128*, **Fig.**
284 **1B**) (Consortium, 2012). Animals lacking FLWR-1 did not display severe phenotypes. Basal
285 locomotion in liquid (**Fig. 1C, D** seconds 0 – 30) and body length of young adults (**Figure 1 – Figure**
286 **supplement 1A**) were not significantly different from the respective values of wild type animals.
287 However, fertility appeared slightly reduced (**Figure 1 – Figure supplement 1B**). Basal crawling
288 speed, on average, was not different between wild type, *flwr-1* mutants and rescued animals (genomic
289 sequence and 2kB promoter; **Figure 1 – Figure supplement 1C**).

290 These findings indicate that FLWR-1 is unlikely to have an essential function in neurotransmission, at
291 least not during basal *in vivo* activity, but rather a regulatory or facilitatory one. Previously we showed
292 that mutations which only weakly affect basal locomotion can severely affect recovery of swimming
293 speed after strong optogenetic stimulation of cholinergic neurons (Yu et al., 2018). We therefore
294 subjected *flwr-1(ok3128)* mutants expressing channelrhodopsin-2 (ChR2; variant H134R), which were
295 treated with the chromophore all-*trans* retinal (ATR), to blue light during swimming (Liewald et al.,
296 2008; Nagel et al., 2005). Photostimulation resulted in a stop of all swimming during the light pulse,
297 followed by a slow recovery in the dark. Indeed, loss of FLWR-1 led to a significantly slowed recovery
298 of swimming locomotion (**Fig. 1C, D**). This could be fully rescued by transgenic expression of genomic
299 *flwr-1* including a two kilobase sequence upstream of the putative start codon, hereafter called *flwr-1p*
300 (as the promoter of *flwr-1*). To further evaluate the involvement of FLWR-1 in neurotransmission, we
301 exposed *flwr-1* mutants to aldicarb. This acetylcholine esterase (AChE) inhibitor induces paralysis due
302 to accumulation of ACh in the synaptic cleft (Blazie and Jin, 2018; Mahoney et al., 2006). Resistance
303 to aldicarb indicates either reduced release or detection of ACh or, alternatively, increased inhibitory
304 signaling (Janosi et al., 2024; Vashlishan et al., 2008). Loss of FLWR-1 led to a significant delay in
305 paralysis indicating an involvement in transmission at the NMJ (**Fig. 1E**). Full rescue of the *flwr-1*
306 mutant phenotypes suggests that expression from the 2 kB fragment of the endogenous promoter fully
307 recapitulates the native expression in the context of NMJ function.

308 **FLWR-1 is expressed in excitable cells and localizes to synaptic vesicles**

309 Invertebrate and vertebrate homologues of FLWR-1 are predicted to be membrane proteins containing
310 four transmembrane helices with both C- and N-termini located in the cytosol (Chang et al., 2018;
311 Rudd et al., 2023; Yao et al., 2009). *In silico* predictions using the FLWR-1 sequence of 166 amino
312 acids suggest evolutionary conservation of the tetraspan structure (**Figure 1 – Figure supplement 2A**)
313 (Hallgren et al., 2022). Accordingly, Alphafold3 predicts a protein structure of FLWR-1 that implies a
314 four helical configuration, with helix lengths that could span biological membranes, and three
315 additional, shorter α-helices (**Figure 1 – Figure supplement 2B**) (Abramson et al., 2024). We sought
316 to determine the cellular as well as subcellular localizations of FLWR-1 by tagging its N-terminus with
317 GFP and expressing the construct using the endogenous promoter (**Fig. 2A – C**). Green fluorescence
318 could be observed in developing embryos in the uterus, as well as in various tissues including neurons,
319 body wall and pharyngeal muscles (**Fig. 2A**). FLWR-1 localized to neurites and cell bodies of nerve
320 ring neurons, representing the central nervous system of the nematode (**Fig. 2B**) (Ward et al., 1975).
321 These results are in agreement with single-cell RNA-sequencing data obtained from *C. elegans* which
322 show near ubiquitous expression of *flwr-1/F20D1.1* (**Figure 1 – Figure supplement 2C**, **Table S3**;
323 Taylor et al. (2021)). The GFP::FLWR-1 fusion protein was functional as demonstrated by rescue of

the swimming phenotype (recovery from cholinergic neuron photostimulation) observed in the *flwr-1* mutant background (**Figure 1 – Figure supplement 2D, E**).

Within muscle cells, FLWR-1 was primarily targeted to the PM (**Fig. 2C**). As its *D. melanogaster* homolog was localized to synaptic vesicles (SVs) (Yao et al., 2009), we wondered whether FLWR-1 would co-localize with known SV markers such as SNB-1 synaptobrevin-1 (Calahorro and Izquierdo, 2018; Nonet, 1999). Indeed, GFP::FLWR-1 fluorescence largely overlapped with co-expressed mCherry::SNB-1 in the dorsal nerve cord (DNC; **Fig. 2D, E**). FLWR-1 further seemed to be enriched in fluorescent puncta in DNC and sublateral nerve cords indicating synaptic localization (**Fig. 2D - F**), however it was not restricted to synaptic regions only, meaning it is likely present also in the PM. Furthermore, we observed moving particles, probably SV precursors, which contained SNB-1 and FLWR-1, travelling along commissures between ventral nerve cord (VNC) and DNC (**Fig. 2F, G** and **Movie S1**). Anterograde transport of these precursors towards synapses depends on kinesin-3/UNC-104 (Hall and Hedgecock, 1991; Klopfenstein and Vale, 2004). We used a reduction-of-function allele (*e1265*) affecting interaction of UNC-104 with its cargo to investigate whether FLWR-1 is actively transported towards synapses (Cong et al., 2021). Indeed, animals lacking functional UNC-104 showed a reduced amount of axonal GFP fluorescence in the nerve ring and DNC while cell bodies were clearly visible (**Figure 1 – Figure supplement 2F**). The ratio of DNC to VNC fluorescence was significantly decreased in *unc-104* mutants suggesting defective anterograde transport (**Fig. 2H**). Distribution of SNB-1 was similarly affected (Cuentas-Condori et al., 2023; Gally and Bessereau, 2003). Together, these results argue that FLWR-1 is expressed in neurons (as well as in muscles and other cell types) and is actively transported towards synapses.

GABAergic signaling is increased in *flwr-1* knockout mutants

Since FLWR-1 is also expressed in body wall muscles (BWMs), we wondered whether the observed aldicarb resistance originates from reduced ACh reception by ACh receptors (AChRs) (Mahoney et al., 2006). To test this, we exposed animals lacking FLWR-1 to levamisole, an AChR agonist which induces paralysis by hyperexcitation and body contraction, similar to aldicarb (Gottschalk et al., 2005; Sattelle et al., 2002). We found no significant differences in the rate of paralysis between wild type and mutant animals (**Figure 1 – Figure supplement 3A**). However, transgenic expression of FLWR-1 in BWMs partially rescued the aldicarb resistance (**Figure 1 – Figure supplement 3B**). Therefore, loss of FLWR-1 might decrease the ACh response of muscle cells, which may contribute to the aldicarb resistance of *flwr-1* mutants. However as muscles can also affect motor neurons by inhibitory retrograde signaling (Hu et al., 2012; Simon et al., 2008; Tong et al., 2017), we wanted to assess if the loss of FLWR-1 in muscle may also have effects on motor neurons. Thus, we rescued FLWR-1 in muscle and either cholinergic or GABergic neurons (**Figure 1 – Figure supplement 3B**). The combined rescues did not show any additive effects to the pure neuronal rescues, thus FLWR-1 effects on muscle cell responses to cholinergic agonists might be cell-autonomous. Yet, as cholinergic rescue alone did not overcompensate *flwr-1* mutants' resistance in aldicarb assays (**Figure 3D**), this interpretation is complicated . Since muscles are activated by ACh via two different AChRs, the levamisole receptor and the nicotine-sensitive receptor (N-AChR), a homopentamer of ACR-16 subunits (Almedom et al. 2009; Richmond and Jorgensen, 1999), we addressed the possibility that FLWR-1 may regulate expression or function of N-AChRs in muscle, to affect phenotypes of aldicarb resistance. We performed aldicarb assay in the absence of the ACR-16 (**Figure 1 – Figure supplement 3C**), which showed that the two mutations, *flwr-1(ok3128)* and *acr-16*(*ok789)*, had additive effects. Thus, FLWR-1 does not affect aldicarb resistance through downregulation of nAChRs, as otherwise the double mutant would not be more resistant than the *flwr-1* single mutant.

369 In addition to muscle expression, we also observed enrichment of FLWR-1 in fluorescent puncta
370 indicating presynaptic localization (**Fig. 3A, B**). Moreover, FLWR-1 partially co-localized with the
371 dense projection marker ELKS-1 in cholinergic, as well as in GABAergic neurons (**Fig. 3A-C**; **Figure**
372 **3 – Figure supplement 1A-C**; Dai et al. (2006); Kittelmann et al. (2013a)). Unlike ELKS-1, FLWR-
373 1 could also be found in intersynaptic regions, though to a lesser extent than in synapses. This indicates
374 that FLWR-1 might be involved in neurotransmission at both cholinergic and GABAergic NMJs, yet
375 is not exclusively localized to active zones. The expression of FLWR-1 relative to ELKS-1 in either
376 neuron type was not obviously biased to GABAergic or cholinergic neurons (**Figure 3 – Figure**
377 **supplement 1A-C**). Thus, to determine whether the site of action of FLWR-1 in NMJ signaling is also
378 evenly located to cholinergic and GABAergic neurons, we rescued FLWR-1 in each cell type of *flwr-*
379 *1* mutants, using the promoters of the vesicular transporters of ACh (UNC-17) or GABA (UNC-47),
380 respectively. Surprisingly, expression of FLWR-1 in GABAergic, but not in cholinergic neurons,
381 rescued aldicarb resistance (**Fig. 3D**). This was unexpected, since mutations affecting SV recycling
382 commonly lead to a slowed replenishment of SVs and thus reduced ACh release (Salcini et al., 2001;
383 Schuske et al., 2003; Yu et al., 2018). However, our results indicate that loss of FLWR-1 leads to
384 increased release of GABA, which counteracts the aldicarb induced paralysis (Camara et al., 2019).
385 Additional expression of FLWR-1 in BWMs did not change these results, suggesting that its role in
386 neurons is more crucial in affecting aldicarb sensitivity (**Figure 1 – Figure supplement 3B**). To
387 confirm this, we crossed *flwr-1* mutants to animals lacking the vesicular GABA transporter UNC-47.
388 This abolishes GABA release and induces hypersensitivity to aldicarb (Vashlishan et al., 2008). We
389 observed that the additional mutation of *unc-47* led to a complete loss of aldicarb resistance in *flwr-1*
390 mutants (**Fig. 3E**). No difference between *unc-47* and *flwr-1; unc-47* double mutants could be
391 observed. However, as we used a high concentration of aldicarb, possible additional effects of the
392 double mutant may have been masked. Thus, we also tested these animals at a lower concentration of
393 aldicarb. *unc-47; flwr-1* double mutants were hypersensitive to aldicarb compared to *unc-47* single
394 mutants, suggesting that ACh release is also increased by the loss of FLWR-1 (**Figure 1 – Figure**
395 **supplement 3D**). In the absence of the compensatory increase in GABAergic signaling, this conveys
396 aldicarb hypersensitivity. Jointly, these findings support the notion that it is primarily increased GABA
397 signaling which is the main cause of aldicarb resistance in *flwr-1* mutants, yet neurotransmission in
398 motor neurons may be generally upregulated.

399 **Depolarization-induced neuronal Ca^{2+} is increased in *flwr-1* mutants**

400 Since the release of GABA appeared to be increased in *flwr-1* mutants, we wondered whether the
401 response of GABAergic neurons during activation was increased. To test this, the fluorescent Ca^{2+}
402 indicator GCaMP was expressed in GABAergic neurons, allowing us to estimate relative Ca^{2+} levels
403 at presynaptic sites (Lu et al., 2022; Nakai et al., 2001). To allow optogenetic depolarization of neurons
404 independent of GCaMP excitation light, we co-expressed the red-shifted channelrhodopsin variant
405 ChrimsonSA (Oda et al., 2018; Seidenthal et al., 2022). As expected, optogenetic stimulation caused
406 an increase in GCaMP fluorescence at NMJs in the DNC (**Fig. 4A**). Comparing wild type and *flwr-1*
407 mutants, we found that the gain in fluorescence intensity was significantly higher in animals lacking
408 FLWR-1 (**Fig. 4A, B**), supporting our finding of increased neurotransmission in GABAergic neurons.
409 To verify this at the behavioral level, we used a strain expressing ChR2(H134R) in GABAergic
410 neurons, as it can be used to assess GABA release through measurement of body length (Liewald et
411 al., 2008). Since GABA receptors hyperpolarize muscle cells, optogenetic stimulation of GABAergic
412 motor neurons causes relaxation and thus increased body length (Schultheis et al., 2011; Seidenthal et
413 al., 2022). To augment the effect of ChR2 stimulation on body length and to observe the effect of
414 GABA release independent of cholinergic neurotransmission, the assay was performed in a mutant

415 background lacking the levamisole receptor (*unc-29(e1072)* mutants, affecting an essential subunit;
416 Fleming et al. (1997); Richmond and Jorgensen (1999)). As expected, stimulation with blue light led
417 to increased body length (**Fig. 4C**). In accordance with Ca^{2+} imaging results, *flwr-1; unc-29* double
418 mutants showed a significantly stronger elongation during stimulation than *unc-29* mutants (**Fig. 4C,**
419 **D**). These results indicate that Ca^{2+} influx into the synaptic cytosol is increased, likely causing more
420 GABA to be released in animals lacking FLWR-1. The previously observed aldicarb resistance
421 indicates that this change in GABAergic transmission outweighs possible changes in cholinergic
422 transmission (**Fig. 3**).

423 To investigate whether neuronal responses to depolarization may be generally upregulated in *flwr-1*
424 mutants, we assessed whether evoked Ca^{2+} level increase is affected in cholinergic motor neurons as
425 well (**Fig. 4E, F**). Again, we observed increased GCaMP fluorescence levels during optogenetic
426 stimulation. This effect could be rescued in cholinergic neurons. However, since postsynaptic muscle
427 exerts inhibitory retrograde signaling to presynaptic cholinergic neurons (Hu et al., 2012; Simon et al.,
428 2008; Tong et al., 2017), and because FLWR-1 is also expressed in muscle, we tested if the phenotype
429 of the loss of FLWR-1 in cholinergic neurons would be affected by rescuing FLWR-1 in muscle. This
430 was not the case (**Fig. 4E, F**). Together, these results indicate that loss of FLWR-1 conveys an
431 upregulation of neuronal Ca^{2+} level rise during continuous stimulation in both classes of motor neurons
432 (**Fig. 4G**). However, the overall E/I balance appears to be shifted towards stronger inhibition of BWMs.

433 **Endocytosis is slowed in *flwr-1* mutants in non-neuronal cells and neurons**

434 Homologues of FLWR-1 were implicated in endocytosis in neurons as well as in non-neuronal cells
435 (Chang et al., 2018; Rudd et al., 2023; Yao et al., 2009). We thus wondered whether this function is
436 evolutionarily conserved in nematodes. One possibility to assess this in *C. elegans* is to observe
437 endocytosis in coelomocytes (CCs; (Fares and Greenwald, 2001). These scavenger cells continuously
438 endocytose fluid from the body cavity and loss of endocytosis-associated factors affects uptake of
439 proteins secreted from other tissues (Fares and Grant, 2002). GFP fused to a secretory signal sequence
440 is discharged from BWMs, and its endocytic uptake by CCs can be quantified by fluorescence
441 microscopy (Bednarek et al., 2007; Fares and Greenwald, 2001). According to single-cell RNAseq
442 data, FLWR-1 is expressed in CCs (**Table S3**; Taylor et al. (2021). Indeed, mutation of *flwr-1* led to
443 strongly reduced GFP fluorescence levels within CCs indicating a reduced uptake by endocytosis (**Fig.**
444 **5A, B**). This defect could be cell-autonomously rescued by expressing FLWR-1 in CCs from the *unc-*
445 *122* promoter. Furthermore, to assess recycling of SVs, we used the pOpsicle (pH-sensitive optogenetic
446 reporter of synaptic vesicle recycling) assay we recently established (Seidenthal et al., 2023) to estimate
447 the amount of SV fusion and the rate of recycling of SV components in cholinergic neurons. This assay
448 combines a pHluorin based probe fused to an SV-associated protein (SNG-1) and optogenetic
449 stimulation of neurotransmitter release; this way, pHluorin fluorescence is unquenched during
450 stimulated exocytosis and quenched during SV endocytosis and recycling (Sankaranarayanan et al.,
451 2000). Since in this assay signals originating from SVs and from the PM contribute to the overall
452 signal, and since FLWR-1 has an effect on endocytosis, we needed to verify that the relative
453 localization of the SNG-1::pHluorin sensor itself was not affected by the *flwr-1* mutation. Basal
454 fluorescence, before stimulation, was unaltered in *flwr-1* mutants, showing that there is no FLWR-1
455 dependent alteration of SNG-1::pHluorin in cellular membranes (**Figure 4 – Figure supplement 1A**).
456 In addition, to estimate the amount of the sensor present in the PM vs. in vesicles, we used primary
457 culture of *C. elegans* cells. Cholinergic neurons expressing SNG-1::pHluorin were imaged and exposed
458 to different pH by adding a buffer of pH 5.6, or by adding ammonium chloride buffer of physiological
459 / neutral pH, which can penetrate the cell and thus shows the maximum achievable signal, i.e. all
460 unquenched pHluorin signal present in the cell. This showed that the amount of SNG-1::pHluorin

461 present in SVs was also not affected by the *flwr-1* mutation (**Figure 4 – Figure supplement 1B, C**).
462 *In vivo*, loss of FLWR-1 led to significantly increased fluorescence signals during stimulation which
463 indicates more SV fusion compared to wild type (**Fig. 5C, E**). This is in accordance with the increased
464 responses of cholinergic neurons to depolarization we observed earlier (**Fig. 4E, F**). Moreover, the rate
465 of fluorescence decay after stimulation was significantly reduced in *flwr-1* mutants suggesting slower
466 recycling of SVs, or reduced acidification of endosomal structures or SVs after recycling (**Fig. 5D, F**).

467 Slowed replenishment of SV pools caused by defective recycling is known to cause synaptic
468 depression, as assessed by electrophysiological measurements of post-synaptic currents (Kittelmann et
469 al., 2013b; Krick et al., 2021; Wu and Betz, 1998). This is also the case in *Drosophila* for animals
470 lacking Flower (Yao et al., 2009). To address this in *C. elegans*, we measured miniature post-synaptic
471 currents (mPSCs; minis) in BWMs (**Fig. 5G**), which reflect the post-synaptic effects of presynaptic
472 neurotransmitter release (Liewald et al., 2008; Weissenberger et al., 2011). Animals lacking FLWR-1
473 showed no significant difference in basal mPSC frequency or amplitude (**Fig. 5H, I; Figure 5 – Figure**
474 **supplement 1A, B**) which is in accordance with FLWR-1 being dispensable in basal swimming
475 locomotion (**Fig. 1C, D**). Similarly, pulsed optogenetic stimulation of cholinergic neurons at different
476 frequencies did not reveal a difference in the measured currents between wild type and mutants (**Figure**
477 **5 – Figure supplement 1C, D**), suggesting that FLWR-1 might be needed only during continuous
478 stimulation. Indeed, *flwr-1* mutants showed an accelerated rundown of the mPSC frequency in BWMs
479 during constant illumination (**Fig. 5G, H**). This is in accordance with a role of FLWR-1 in SV
480 recycling. Surprisingly, mPSC amplitudes in *flwr-1* mutants are reduced during 30 s hyperstimulation
481 (**Fig. 5I, J**). This suggests that either the amount of neurotransmitter released from a single SV, or the
482 number of multivesicular fusion events, is decreased (Liu et al., 2005). The absolute mPSC frequency,
483 which represents the number of SVs fusing per time, was also smaller during continuous stimulation
484 in *flwr-1* animals (**Figure 5 – Figure supplement 1E-G**). These results contrast the increased Ca^{2+}
485 responses of cholinergic neurons we observed (**Fig. 4E, F**). Since cholinergic neurons also stimulate
486 GABAergic neurons, and since GABAergic minis are also evaluated here, the dissection of animals,
487 required for electrophysiological recordings, could have damaged neuronal commissures, causing an
488 interruption of physiological signal transmission, which is otherwise observed in intact animals. We
489 further analyzed whether *flwr-1* mutants can recover from strong optogenetic 30 s stimulation by
490 applying a short stimulus after a recovery period (inter-stimulus interval, ISI) of 15 s, and found no
491 significant difference to wild type (**Figure 5 – Figure supplement 1E, H**). This suggests that a 15 s
492 ISI is sufficient for *flwr-1* mutants to recover to the same extent as wild type synapses. In sum, our
493 results support a facilitatory role of FLWR-1 in SV recycling specifically during continuous
494 stimulation.

495 **Loss of FLWR-1 leads to depleted SV pools and accumulation of endocytic structures post**
496 **stimulation**

497 Mutants in which endocytosis is affected commonly have fewer SVs because of defective recovery of
498 SV components; this was also found for presynaptic boutons in *Drosophila* mutants lacking Flower
499 (Schuske et al., 2003; Yao et al., 2009). Such a defect is even more pronounced when samples are
500 conserved immediately following optogenetic stimulation by high-pressure freezing (Kittelmann et al.,
501 2013b; Weimer, 2006; Yu et al., 2018). In nematodes, this optogenetic stimulation can be controlled
502 by comparing animals supplemented with ATR, the ChR2 chromophore (Nagel et al., 2005), to animals
503 without ATR. Ultrastructural analysis using transmission electron microscopy (TEM) indeed revealed
504 fewer SVs in stimulated *flwr-1* mutant synapses compared to wild type (**Fig. 6A, B**). This indicates
505 that *flwr-1* mutants, unlike wild type, are unable to refill SV pools sufficiently fast. At the same time,

506 *Drosophila* Flower mutants were shown to be defective in formation of bulk endosomal structures after
507 strong stimulation (Yao et al., 2017). In contrast to this, we observed an increased, rather than
508 decreased, number of endocytic structures (large vesicles / '100 nm vesicles') in stimulated *flwr-1*
509 mutant synapses (**Fig. 6C**), that were of larger size (**Figure 6 – Figure supplement 1B**). This may
510 either be caused by increased SV fusion which triggers bulk endosomal formation (Clayton et al., 2008;
511 Wu et al., 2014) or defective breakdown of these endocytic structures (Gan and Watanabe, 2018;
512 Watanabe et al., 2013; Yu et al., 2018). Previously, we observed the formation of very large endocytic
513 structures in mutants that affect their resolution into SVs, like endophilin or synaptojanin (Kittelmann
514 et al., 2013b), while a dynamin mutant showed unresolved endocytic structures at, and in continuity
515 with, the PM. Our pHluorin imaging data (**Fig. 5C - F**), would support the notion that both, increased
516 SV fusion as well as defective recovery and subsequent acidification of SVs, may cause the higher
517 number of endocytic structures in *flwr-1* mutants. However, we note that our stimulation regime likely
518 resembles a more physiological activation of neurotransmission compared to the intense stimuli
519 previously used (Yao et al., 2017), as wild type synapses only rarely contained endocytic structures
520 (Kittelmann et al., 2013b). Moreover, we observed fewer docked vesicles in *flwr-1* animals which have
521 been treated with ATR, compared to those without (**Fig. 6D**). This might be caused by increased SV
522 fusion and is in line with the increased Ca^{2+}-levels during stimulation we observed before. The number
523 of neuropeptide-containing dense core vesicles (DCVs) was unchanged in animals lacking FLWR-1
524 (**Figure 6 – Figure supplement 1A**).

525 **The increased Ca^{2+}-levels of *flwr-1* neurons may be caused by deregulation of MCA-3**

526 While a facilitating role of Flower in endocytosis appears to be conserved in *C. elegans*, in contrast to
527 previous findings from *Drosophila* (Yao et al., 2009), we found no evidence that FLWR-1 conducts
528 Ca^{2+} upon insertion into the PM. On the contrary, presynaptic Ca^{2+} levels were increased during
529 photostimulation of neurons in animals lacking FLWR-1. We thus wondered whether clearance of Ca^{2+}
530 which has entered the synapse via VGCCs, might be defective in *flwr-1* mutants. In neurons and
531 muscles, the plasma membrane Ca^{2+} ATPase (PMCA) is involved in extruding Ca^{2+} from the cell
532 (Boczek et al., 2019; Krebs, 2022; Krick et al., 2021). The *C. elegans* homolog MCA-3 (also known
533 as CUP-7) is expressed in neurons, muscle cells and CCs (**Figure 7 – Figure supplement 1A**, **Table**
534 **S3**; Bednarek et al. (2007); Taylor et al. (2021)). Interestingly, reducing the function of MCA-3 by
535 mutation was shown to cause a similar defect in endocytosis of secreted GFP in CCs as the loss of
536 FLWR-1 does (**Fig. 5A, B**; Bednarek et al. (2007)). We therefore wondered whether MCA-3 might be
537 negatively affected in *flwr-1* mutants. To assess this, we used a mutant *mca-3(ok2048)* lacking part of
538 the C-terminal, regulatory calmodulin-binding domain (Consortium, 2012; Kraev et al., 1999; Mantilla
539 et al., 2023) **Fig. 7A**). Since *mca-3* loss-of-function (l.o.f.) mutants are lethal, it is likely that this
540 represents a reduction-of-function (r.o.f.) mutation (Bednarek et al., 2007). As expected, *mca-3*
541 mutants displayed increased Ca^{2+} influx (or net Ca^{2+} levels, representing the summed VGCC-mediated
542 entry and MCA-3-mediated efflux) upon optogenetic stimulation of cholinergic motor neurons, similar
543 to the effect of the *flwr-1* mutation (**Fig**. **7B, C**). Elevated Ca^{2+} levels were not further enhanced in a
544 *flwr-1; mca-3* double mutant. Our data suggest that the two genes are acting in a common pathway. A
545 partially different picture was observed in aldicarb assays, as reduction of MCA-3 function conveyed
546 aldicarb resistance that was, however, less pronounced than for *flwr-1* mutants (**Fig. 7D**). Nevertheless,
547 since the double mutant showed no exacerbated phenotype compared to the *flwr-1* mutant, both
548 proteins appear to function in the same pathway. If MCA-3 function was augmented by FLWR-1, then
549 the loss of FLWR-1 may be overcome by higher MCA-3 expression. Since the main focus of FLWR-
550 1 was the GABAergic NMJ (**Fig. 3D, E**), we analyzed aldicarb resistance in *flwr-1* mutants in which
551 we overexpressed MCA-3 in GABAergic neurons (**Figure 7 – Figure supplement 1B**). Indeed, MCA-
552 3 overexpression in GABAergic neurons efficiently rescued the *flwr-1* resistance to wild type levels.

553 **FLWR-1 structure prediction does not imply Ca^{2+} conducting ability but PI(4,5)P_2 binding**

554 We observed increased rather than decreased Ca^{2+} levels during stimulation, which contrasts findings
555 from *D. melanogaster* Flower (Yao et al., 2017). Previously, an evolutionarily conserved glutamate
556 residue (E78 in the *Drosophila* protein) within the transmembrane domain, which was found to be
557 essential for *Drosophila* Flower function, was suggested to represent a Ca^{2+} selectivity filter because
558 of similarities to $Ca_v1.2$ and TRP channels (Yao et al., 2009). This group proposed that Flower, like
559 TRP channels, can form homo-tetramers to conduct Ca^{2+} (Hoenderop et al., 2003; Yao et al., 2009;
560 Zhang et al., 2023). We therefore wondered whether loss of the conserved glutamate residue impacts
561 FLWR-1 function in *C. elegans* (**Fig. 8A**). Expressing a mutant variant of FLWR-1 in which glutamate
562 74 is exchanged to glutamine (E74Q) significantly decreased the aldicarb resistance of the *flwr-1*
563 mutant (**Fig. 8B**), yet did not fully rescue it. This suggests that the respective glutamate is not essential
564 for *C. elegans* FLWR-1 function. To get more insight into the putative structure and oligomerization
565 of FLWR-1, we used Alphafold 3 (AF3) predictions to estimate the approximate location of the
566 conserved glutamate residue within a putative FLWR-1 homo-tetramer (Abramson et al., 2024; Evans
567 et al., 2022). One of the predicted complexes indeed revealed a pore-like structure (**Figure 8 – Figure**
568 **supplement 1A**). However, while conventional Ca^{2+}-channels contain a glutamate residue within their
569 pore domain (Chen et al., 2023), E74 of FLWR-1 is not predicted to be part of pore-lining residues in
570 the putative tetramer (**Figure 8 – Figure supplement 1B**).

571 Flower, like MCA-3, was also suggested to bind to phosphatidylinositol-4,5-bisphosphate (PI(4,5)P_2),
572 an important regulator of endo/exocytosis and thus SV recycling, and to affect its levels within the PM
573 (Bednarek et al., 2007; Li et al., 2020; Lopreiato et al., 2014). Binding of transmembrane proteins
574 (including TRP channels) to PI(4,5)P_2 is generally mediated by positively charged amino acid residues
575 (lysine and arginine) close to the intracellular side of the PM, which bind to the negatively charged
576 phosphate residues (**Figure 8 – Figure supplement 1C;** (Duncan et al., 2020; Hansen et al., 2011;
577 Ribalet et al., 2005; Rohacs, 2024). The predicted FLWR-1 structure similarly contains basic amino
578 acids which are likely to be close to the intracellular PM leaflet (**Figure 8 – Figure supplement 1D**).
579 We used *in silico* docking prediction to estimate how PI(4,5)P_2 may bind to FLWR-1. In the resulting
580 structure, both phosphate residues are close to lysine 31 and arginine 27 (**Figure 8 – Figure**
581 **supplement 1D**). A positive charge at this position is evolutionarily conserved, suggesting an
582 important function (**Fig. 8A**). Moreover, these amino acids have been suggested to mediate PI(4,5)P_2
583 binding in *D. melanogaster* Flower (Li et al., 2020). Expression of a mutated version of FLWR-1 in
584 which both residues were replaced by alanine only partially rescued aldicarb resistance (**Fig. 8B**),
585 implying that FLWR-1 function may be facilitated by these residues and their potential interaction with
586 PI(4,5)P_2. These findings implicate that the conserved E74 is not essential, yet still important for
587 FLWR-1 activity. In addition, an interaction with PI(4,5)P_2 *via* basic amino acids also seems to be an
588 important factor. However, we do note that FLWR-1 structural models as depicted here rely on *in silico*
589 predictions. The actual biological structure of FLWR-1, or its homologues, has yet to be determined
590 using X-ray crystallography or cryo-EM.

591 The pleckstrin homology (PH) domain of phospholipase Cδ (PLCδ) fused to GFP can be used to
592 estimate PI(4,5)P_2 levels within cells (Botelho et al., 2000; Chen et al., 2014; Stauffer et al., 1998).
593 This was used to show that reduction of MCA-3 function induced decreased PH-PLCδ-GFP
594 fluorescence levels in CCs (Bednarek et al., 2007). We thus used this assay to assess the role of FLWR-
595 1 in endosomal PI(4,5)P_2 levels in CCs. Mutation of *flwr-1* reduced the observed GFP fluorescence
596 suggesting that FLWR-1 positively affects PI(4,5)P_2 levels (**Fig. 8C, D**). We further asked if the
597 putative PI(4,5)P_2 binding site mutations would affect binding of the reporter to the CC membrane. In

598 fact, while expressing FLWR-1 specifically in CCs fully rescued the GFP levels at the CC membrane,
599 expressing the FLWR-1(R27A/K31A) double mutant did not rescue the phenotype, while the E74Q
600 mutant was not significantly different to wild type (**Fig. 8C, D**). These findings indicate that FLWR-1
601 function affects MCA-3 activity through an interaction via $PI(4,5)P_2$ and that FLWR-1 may have an
602 influence on $PI(4,5)P_2$ levels.

603 **A putative direct interaction of FLWR-1 and MCA-3 may increase MCA-3 function dynamically**

604 Next, we asked how FLWR-1 may affect MCA-3 through $PI(4,5)P_2$, and whether this may involve
605 proximity of the two proteins. To test this, we used Bimolecular Fluorescence Complementation
606 (BiFC) *in vivo*. This assay uses two non-fluorescent fragments of mVenus (VN173 and VC155,
607 respectively), which can recombine and complement each other to form a fluorescent protein, as long
608 as they come into close proximity within the cell (Almedom et al., 2009; Chen et al., 2007; Hu et al.,
609 2002). The fragments can be fused to putative interaction partners and fluorescence complementation
610 (including a covalent bond formation in the reconstituted fluorophore) verifies interaction. We thus
611 fused the VC155 fragment to the C- terminus of FLWR-1 and the VN173 fragment to the C-terminus
612 of MCA-3, and co-expressed both proteins (FLWR-1 was expressed from its own promoter, while
613 MCA-3 was expressed in BWM cells; **Fig. 9A**). Fluorescence could readily be observed at the PM of
614 muscles cells, but not in other tissues that also express FLWR-1 (**Fig. 9B**). As a control, we used two
615 other proteins for probing interactions with FLWR-1: First, the ER-membrane protein NRA-2, which
616 is a homologue of mammalian Nicalin, a component of the translocon-associated Nicalin-TMEM147-
617 NOMO complex that assists folding and assembly of multipass transmembrane proteins in the ER
618 (McGilvray et al., 2020; Smalinskaitė et al., 2022). We previously showed interactions of
619 Nicalin/NRA-2 and the NOMO homologue NRA-4 by BiFC (Almedom et al., 2009). We would expect
620 that FLWR-1, as a multipass TM protein, would also get into close proximity with the NRA-2/Nicalin
621 protein upon biogenesis. Indeed, a clear ER-localized signal was observed when probing FLWR-
622 1::VC155 and NRA-2::VN173 interactions in muscle (**Fig. 9. B**). Second, to exclude that FLWR-1
623 would interact with any protein presented in the BiFC assay, we used the UNC-1 stomatin, that is
624 associated with innexin gap junctions in neurons and muscles (Chen et al., 2007). Co-expressing
625 FLWR-1::VC155 with UNC-1::VN173 in BWMs, however, did not lead to distinct YFP reconstitution,
626 apart from some general dim fluorescence that was hardly above the level of autofluorescence (**Fig.
627 9B**). These findings indicate that FLWR-1 and MCA-3 may interact with each other in the PM. If this
628 interaction is functional, linking the two proteins via BiFC may not have adverse effects on either
629 protein. We thus tested the transgenic animals in swimming assays (**Figure 9 – Figure supplement
630 1**). Neither expression of FLWR-1 with MCA-3 or FLWR-1 with NRA-2 affected swimming
631 locomotion, showing that there were no dominant negative effects. Note that wild type FLWR-1 and
632 MCA-3 were present in these animals. However, as *mca-3* mutants have a significant reduction in
633 swimming ability (**Figure 9 – Figure supplement 1**), the fact that FLWR-1/MCA-3 BiFC had no
634 adverse effects, indicates that the physical interaction of the two proteins is in line with their native
635 function.

636 These observations indicate that MCA-3 and FLWR-1 may be interacting directly, and thus their
637 function may jointly be responsible for the Ca^{2+}-induced recycling of SVs. Since the increased Ca^{2+}
638 levels in neurons upon stimulation in *flwr-1* mutants may reflect altered MCA-3 abundance at synapses,
639 we tested if FLWR-1 would affect localization of MCA-3 along neuronal membranes. We expressed
640 MCA-3b::YFP in cholinergic neurons, which was observable along axonal membranes and was
641 enriched in synaptic specializations (**Fig. 9C**). In *flwr-1* mutants, this synaptic fluorescence was not
642 overall altered (**Fig. 9D**), however, when we compared the YFP signals within the synaptic
643 specializations relative to the inter-synaptic axon shafts, this demonstrated a significantly reduced

644 presence of MCA-3 in synaptic puncta and a relocation to the axonal membranes (**Fig. 9E**). This is in
645 line with the idea that FLWR-1 function may stabilize / augment MCA-3 expression in the plasma
646 membrane and / or its localization in synaptic puncta, to promote efficient synaptic function and SV
647 recycling.

648 Discussion

649 *Drosophila* Flower was shown to affect SV recycling and to alter synaptic Ca^{2+} levels upon stimulation.
650 It was suggested to form a Ca^{2+} channel that gets inserted into the plasma membrane upon SV fusion.
651 Here, we showed that also in *C. elegans*, FLWR-1 affects synaptic Ca^{2+} levels following stimulation,
652 that FLWR-1 is localized to SVs in neuronal cells, and that in its absence, endosomal structures with
653 slowed acidification kinetics accumulate, suggesting defective recovery of SVs from recycling
654 endosomes. FLWR-1 may affect SV recycling by stimulating the PMCA MCA-3, possibly by directly
655 interacting with it, and *via* modulation of $PI(4,5)P_2$ levels, may affect the abundance of MCA-3 in the
656 synaptic membrane. We found that loss of FLWR-1 conveyed increased Ca^{2+} entry into the motor
657 neuron cytosol, particularly GABAergic neurons, thus leading to more GABA release, an E/I
658 imbalance at the NMJ, and leading to aldicarb resistance. Since the *C. elegans* NMJ comprises
659 cholinergic and GABAergic neurons, and the aldicarb assay relies on muscle contraction, interpreting
660 results is complicated if a given mutation affects the two motor neuron types (or muscle physiology)
661 differently. We thus included cell-type specific rescue in our analyses. The function of FLWR-1
662 appears to be ubiquitously involved in membrane trafficking and PM-endosomal recycling, as we
663 found it to affect endocytosis and PM $PI(4,5)P_2$ levels also in coelomocytes. Our findings are
664 summarized in a model in **Fig. 10**.

665 MCA-3 was shown to facilitate endocytosis in CCs (Bednarek et al., 2007), indicating that both,
666 increased Ca^{2+} levels as well as defective endocytosis may be influenced by deregulation / lack of
667 stimulation of MCA-3 in *flwr-1* mutants. Whether FLWR-1 directly modulates localization or activates
668 function of MCA-3, or whether this is caused by a homeostatic change in the absence of FLWR-1, is
669 unclear as yet. Our finding of a putative direct interaction of FLWR-1 with MCA-3 suggests that
670 FLWR-1 could be inserted into the PM to stimulate activity of MCA-3 already present in the PM.
671 Alternatively, MCA-3 may undergo dynamic PM insertion and endocytic recycling as part of SVs,
672 along with FLWR-1 (mammalian PMCA was indeed found in purified SVs; (Takamori et al., 2006).
673 In synapses, this would automatically happen upon SV fusion, such that local Ca^{2+} extrusion at release
674 sites would ensure synapse functionality during intense activity. Such a function of PMCA was shown
675 in *Drosophila*, where PMCA domains delineate areas of SV fusion from areas of SV endocytosis
676 (Krick et al., 2021). Thus, independent Ca^{2+} signaling in these two domains, *via* the P/Q type Ca^{2+}
677 channel Ca_v2 (UNC-2 in *C. elegans*) and the L-type Ca_v1 (EGL-19 in *C. elegans*), mediating fusion
678 and endocytosis, respectively, are facilitated by the PMCA. MCA-3 could be acutely regulated by
679 FLWR-1, in addition to its regulation by phospholipids (Lopreiato et al., 2014). Proof of a direct
680 physical interaction will have to be confirmed by biochemical assays and a biological structure of the
681 putative FLWR-1/MCA-3 complex.

682 *Drosophila* Flower was shown to increase neuronal $PI(4,5)P_2$ levels, driving ADBE during sustained
683 transmission (Li et al., 2020). We could show that an involvement with $PI(4,5)P_2$ is likely conserved
684 in nematodes, requiring the putative $PI(4,5)P_2$ binding site residues R27 and K31 of FLWR-1.
685 Similarly, MCA-3 was important to maintain $PI(4,5)P_2$ in CCs (Bednarek et al., 2007). Thus, FLWR-
686 1 and MCA-3 may have a shared role in regulating $PI(4,5)P_2$ levels, or FLWR-1 PM insertion stabilizes
687 local $PI(4,5)P_2$. Recently, another SV protein, synaptotagmin1 (Syt1), it was shown to influence

688 synaptic PI(4,5)P_2 levels following inserts fusion, by recruiting PIP kinase I gamma (PIPKIγ) (Bolz et
689 al., 2023). Syt1 provides a binding site for PIPKIγ, involving R322 and K326, as part of the sequence
690 **R**LKK**K**. In FLWR-1, R27 and K31 are part of the sequence **R**FLA**K**.

691 Our results indicate that MCA-3 may be functionally affected / not stimulated in *flwr-1* mutants,
692 explaining increased Ca^{2+} levels during neuronal stimulation (Brini and Carafoli, 2011; Chamberland
693 et al., 2019; Ono et al., 2019). The increased Ca^{2+} level increase we observed was at first surprising,
694 since work in *Drosophila* yielded opposite results during 40 Hz electrical stimulation in neuromuscular
695 boutons of Flower mutants (Yao et al., 2017). Upon stimulation with 10 Hz, however, these animals
696 showed an increased GCaMP signal compared to wild type, in line with our observations. Potentially,
697 increased Ca^{2+} in *flwr-1* mutants is only observed with lower, more physiological stimulation.
698 Stimulation by ChrimsonSA, which we used in the Ca^{2+} imaging assays, is not as vigorous, thus we
699 are likely in a regime comparable to the 10 Hz stimulation in *Drosophila*. Using stronger stimulation
700 *via* ChR2(H134R), as in the electrophysiological assays, led to a prominent rundown of evoked
701 amplitudes. This may be a consequence of lower Ca^{2+} levels, and interference of MCA-3 with UNC-2
702 dependent Ca^{2+} microdomains required for exocytosis, leading to less fusion events. During intense
703 stimulation, larger amounts of PMCA/MCA-3 may be inserted into the PM due to the high number of
704 SVs fusing. Without FLWR-1, less PI(4,5)P_2 is generated and thus MCA-3 may not be effectively
705 recycled from the PM, thus leading to reduced Ca^{2+} levels as observed in *Drosophila*.

706 Even though we observed increased instead of decreased Ca^{2+} level increase in *flwr-1* mutants, in line
707 with a stimulatory effect of FLWR-1 on MCA-3, we cannot exclude a possible Ca^{2+}-conductivity of
708 FLWR-1. It was discussed that the kinetics of Ca^{2+} levels rising, induced by Flower in *Drosophila*, are
709 too slow and the extent too little as to directly trigger known modes of endocytosis (Brose and Neher,
710 2009; Leitz and Kavalali, 2016; Xue et al., 2012), e.g. by activating the Ca^{2+} sensor calmodulin (Wu
711 et al., 2009). To assess the possibility of FLWR-1 forming an ion channel we asked AlphaFold3 to
712 model FLWR-1 as a tetramer. The putative pore lining residues were mostly hydrophobic or apolar,
713 thus not in agreement with a function as an ion channel. The suggested similarity to the selectivity filter
714 of VGCCs, including the sequence EGW or EAW (in FLWR-1 this is EAP; Yao et al., 2009) was not
715 confirmed in the AF3 models: While glutamate faces the extracellular end of the VGCC pore in all
716 four channel modules, $E74_{FLWR-1}$ pointed away from the pore. We thus think that FLWR-1 is unlikely
717 to form an ion channel, and suggest that it facilitates SV recycling by stimulating MCA-3 activity.

718 Activating PMCAs *via* PI(4,5)P_2 (Berrocal et al., 2017) would remove Ca^{2+} and prevent sustained
719 phospholipase C activity, thus protecting PI(4,5)P_2 at the PM from hydrolysis (Lopreiato et al., 2014;
720 Penniston et al., 2014), and activating different forms of endocytosis (Blumrich et al., 2023; Bolz et
721 al., 2023; Posor et al., 2015). Such interactions could further trigger a positive feedback loop leading
722 to invagination of the PM (Yao et al., 2017). Both PMCAs and Flower were suggested to directly bind
723 PI(4,5)P_2 using positively charged amino acid residues close to the membrane (Filoteo et al., 1992; Li
724 et al., 2020). In line with this, the FLWR-1 structure model exhibits amino acids in suitable positions.
725 This could lead to a close arrangement of both proteins in PI(4,5)P_2 lipid microdomains (Katan and
726 Cockcroft, 2020). Flower could also activate PMCAs in intracellular compartments. One PMCA
727 variant was shown to mainly localize to recycling SVs and endosomes, and Ca^{2+} entry into these is an
728 important factor in clearance from the pre-synapse (Ono et al., 2019). Overall, this may explain our
729 finding of increased numbers of large endocytic structures in *flwr-1* synapses. Effects of *flwr-1*
730 mutations on PI(4,5)P_2 at the PM may negatively affect ADBE, while effects on PI(4,5)P_2 in bulk
731 endosomes may slow the breakdown of these structures (**Fig. 10**). Our ultrastructural analysis contrasts
732 EM analyses in *Drosophila* which yielded fewer, rather than more, bulk endosomal structures in Flower
733 mutants (Li et al., 2020; Yao et al., 2017). However, this was following prolonged (ten minute)

734 stimulation, possibly resulting in different outcomes compared to our 30 s optogenetic stimulus.
735 Alternatively, the subcellular localization of Flower function may differ between organisms.

736 Last, Flower could facilitate endocytosis through calcineurin (Yao et al., 2017), to stimulate bulk
737 endosome formation. This Ca^{2+}- and calmodulin-dependent phosphatase dephosphorylates endocytic
738 proteins to accelerate SV recycling (Cousin and Robinson, 2001; Kumashiro et al., 2005; Yamashita,
739 2012). How could the increased Ca^{2+} levels in the absence of FLWR-1 and the decreased rate of
740 pHluorin decay fit to this idea? Possibly, increased activation of calcineurin shifts the endocytic mode
741 from ultrafast endocytosis (UFE) (Watanabe et al., 2013) to ADBE (Kittelmann et al., 2013b;
742 Yamashita, 2012). Structures formed by bulk endocytosis are acidified more slowly than small
743 endocytic vesicles generated by UFE, which could explain the delayed decay of pHluorin fluorescence
744 (Gross and von Gersdorff, 2016; Okamoto et al., 2016). More pronounced neurotransmission, due to
745 increased SV fusion, causes an increase in bulk invaginations (Clayton et al., 2008), yet the endocytic
746 structures formed this way are not efficiently disassembled. The *C. elegans* calcineurin TAX-6 is
747 further involved in activity-dependent bulk endocytic processes, yet in a different context, i.e.
748 reorganization of GABAergic synapses during development (Cuentas-Condori et al., 2023; Miller-
749 Fleming et al., 2016). The remote possibility that FLWR-1 also takes part in this process could imply
750 that developmental aspects of FLWR-1 function may influence E/I balance in adult NMJs.

751 In sum, our work confirms a conserved role of FLWR-1 in neurotransmission and SV recycling even
752 though we observed differences to data from *Drosophila* NMJs. We found an unexpected upregulation
753 of neurotransmission in *flwr-1* mutants which has not yet been observed in other animals, and which
754 may result from FLWR-1 acting on PMCAs directly. The observed reduced Ca^{2+} levels in hyper-
755 stimulated *Drosophila* synapses may instead result from 'stranded' PMCA in the PM, due to impaired
756 recycling, thus increasing Ca^{2+} extrusion. Further investigations are required to confirm involvement
757 of FLWR-1 in MCA-3 regulation and the nature of the relationship between these proteins.

758 Author Contributions

759 MS created plasmids. MS and NS generated strains. MS performed light microscopy, swimming
760 assays, pharmacological assays and body length measurements. SS conducted aldicarb assays. JR and
761 DR prepared EM samples and conducted EM experiments. JL performed electrophysiology. NR
762 generated primary neuronal cell cultures. MS and AG designed and coordinated the study. MS and AG
763 wrote the manuscript. AG and SE supervised the work and acquired funding. All authors read and
764 approved the final manuscript.

765 Funding

766 This project was funded by Deutsche Forschungsgemeinschaft, Collaborative Research Centre 1080
767 project B02 (grants CRC1080/B2 and GO1011/13-2), as well as by core funding from Goethe
768 University.

769 Acknowledgments

770 We are indebted to Katharina Kuhlmeier for expert technical assistance, and members of the Gottschalk
771 group for critical comments regarding the manuscript. We further thank Martina Rudgalvyte from the
772 Glauser Lab (Université de Fribourg) for helpful comments. We express our gratitude to members of
773 the Zimmer Lab (University of Vienna) for providing advice and plasmids for GCaMP imaging, and
774 to the Wang Lab (University of Connecticut), as well as the Zhen lab (University of Toronto) for

775 providing plasmids. Some deletion mutations used in this work were provided by the International *C.*
776 *elegans* Gene Knockout Consortium (*C. elegans* Gene Knockout Facility at the Oklahoma Medical
777 Research Foundation, which is funded by the National Institutes of Health, and the *C. elegans* Reverse
778 Genetics Core Facility at the University of British Columbia, which is funded by the Canadian Institute
779 for Health Research, Genome Canada, Genome B.C., the Michael Smith Foundation, and the National
780 Institutes of Health). Finally, we thank the *Caenorhabditis* Genetics Center (CGC), which is funded
781 by the NIH Office of Research Infrastructure Programs (P40 OD010440), for providing strains.

782 **References**

783 Abramson, J., Adler, J., Dunger, J., Evans, R., Green, T., Pritzel, A., Ronneberger, O., Willmore, L., Ballard, A.J.,
784 Bambrick, J., *et al.* (2024). Accurate structure prediction of biomolecular interactions with AlphaFold 3. Nature *630*, 493-
785 500.

786 Alabi, A.A., and Tsien, R.W. (2012). Synaptic vesicle pools and dynamics. Cold Spring Harb Perspect Biol *4*, a013680.

787 Almedom, R.B., Liewald, J.F., Hernando, G., Schultheis, C., Rayes, D., Pan, J., Schedletzky, T., Hutter, H., Bouzat, C.,
788 and Gottschalk, A. (2009). An ER-resident membrane protein complex regulates nicotinic acetylcholine receptor subunit
789 composition at the synapse. EMBO J *28*, 2636-2649.

790 Aoki, I., Golinelli, L., Dunkel, E., Bhat, S., Bassam, E., Beets, I., and Gottschalk, A. (2024). Hierarchical regulation of
791 functionally antagonistic neuropeptides expressed in a single neuron pair. Nat Commun *15*, 9504.

792 Bednarek, E.M., Schaheen, L., Gaubatz, J., Jorgensen, E.M., and Fares, H. (2007). The plasma membrane calcium ATPase
793 MCA-3 is required for clathrin-mediated endocytosis in scavenger cells of Caenorhabditis elegans. Traffic *8*, 543-553.

794 Berrocal, M., Corbacho, I., Sepulveda, M.R., Gutierrez-Merino, C., and Mata, A.M. (2017). Phospholipids and calmodulin
795 modulate the inhibition of PMCA activity by tau. Biochim Biophys Acta Mol Cell Res *1864*, 1028-1035.

796 Bhatla, N. (2012). Exon-Intron Graphic Maker. Available at http://wormweb.org/exonintron.

797 Blazie, S.M., and Jin, Y. (2018). Pharming for Genes in Neurotransmission: Combining Chemical and Genetic Approaches
798 in Caenorhabditis elegans. ACS Chem Neurosci *9*, 1963-1974.

799 Blumrich, E.M., Nicholson-Fish, J.C., Pronot, M., Davenport, E.C., Kurian, D., Cole, A., Smillie, K.J., and Cousin, M.A.
800 (2023). Phosphatidylinositol 4-kinase IIalpha is a glycogen synthase kinase 3-regulated interaction hub for activity-
801 dependent bulk endocytosis. Cell reports *42*, 112633.

802 Boczek, T., Radzik, T., Ferenc, B., and Zylinska, L. (2019). The Puzzling Role of Neuron-Specific PMCA Isoforms in the
803 Aging Process. Int J Mol Sci *20*.

804 Bolz, S., Kaempf, N., Puchkov, D., Krauss, M., Russo, G., Soykan, T., Schmied, C., Lehmann, M., Müller, R., Schultz, C.,
805 *et al.* (2023). Synaptotagmin 1-triggered lipid signaling facilitates coupling of exo- and endocytosis. Neuron *111*, 3765-
806 3774.e3767.

807 Botelho, R.J., Teruel, M., Dierckman, R., Anderson, R., Wells, A., York, J.D., Meyer, T., and Grinstein, S. (2000).
808 Localized biphasic changes in phosphatidylinositol-4,5-bisphosphate at sites of phagocytosis. J Cell Biol *151*, 1353-1368.

809 Brenner, S. (1974). The genetics of Caenorhabditis elegans. Genetics *77*, 71-94.

810 Brini, M., and Carafoli, E. (2011). The plasma membrane Ca(2)+ ATPase and the plasma membrane sodium calcium
811 exchanger cooperate in the regulation of cell calcium. Cold Spring Harb Perspect Biol *3*.

812 Brose, N., and Neher, E. (2009). Flowers for synaptic endocytosis. Cell *138*, 836-837.

813 Calahorro, F., and Izquierdo, P.G. (2018). The presynaptic machinery at the synapse of C. elegans. Invert Neurosci *18*, 4.

814 Calhoun, A.J., Chalasani, S.H., and Sharpee, T.O. (2014). Maximally informative foraging by Caenorhabditis elegans.
815 eLife *3*.

816 Camara, D.F., Machado, M.L., Arantes, L.P., Silva, T.C., Silveira, T.L., Leal, J.G., Dornelles, L., Stefanello, S.T., and
817 Soares, F.A.A. (2019). MPMT-OX up-regulates GABAergic transmission and protects against seizure-like behavior in
818 Caenorhabditis elegans. Neurotoxicology *74*, 272-281.

819 Chamberland, S., Zamora Moratalla, A., and Topolnik, L. (2019). Calcium extrusion mechanisms in dendrites of mouse
820 hippocampal CA1 inhibitory interneurons. Cell Calcium *77*, 49-57.

821 Chanaday, N.L., Cousin, M.A., Milosevic, I., Watanabe, S., and Morgan, J.R. (2019). The Synaptic Vesicle Cycle
822 Revisited: New Insights into the Modes and Mechanisms. The Journal of Neuroscience *39*, 8209-8216.

823 Chang, H.F., Mannebach, S., Beck, A., Ravichandran, K., Krause, E., Frohnweiler, K., Fecher-Trost, C., Schirra, C., Pattu,
824 V., Flockerzi, V.*, et al.* (2018). Cytotoxic granule endocytosis depends on the Flower protein. J Cell Biol *217*, 667-683.

825 Chen, B., Liu, Q., Ge, Q., Xie, J., and Wang, Z.W. (2007). UNC-1 regulates gap junctions important to locomotion in C.
826 elegans. Curr Biol *17*, 1334-1339.

827 Chen, C.K., Bregere, C., Paluch, J., Lu, J.F., Dickman, D.K., and Chang, K.T. (2014). Activity-dependent facilitation of
828 Synaptojanin and synaptic vesicle recycling by the Minibrain kinase. Nature communications *5*, 4246.

829 Chen, Z., Mondal, A., Abderemane-Ali, F., Jang, S., Niranjan, S., Montano, J.L., Zaro, B.W., and Minor, D.L., Jr. (2023).
830 EMC chaperone-Ca(V) structure reveals an ion channel assembly intermediate. Nature *619*, 410-419.

831 Clayton, E.L., Evans, G.J., and Cousin, M.A. (2008). Bulk synaptic vesicle endocytosis is rapidly triggered during strong
832 stimulation. J Neurosci *28*, 6627-6632.

833 Coelho, D.S., and Moreno, E. (2020). Neuronal Selection Based on Relative Fitness Comparison Detects and Eliminates
834 Amyloid-beta-Induced Hyperactive Neurons in Drosophila. iScience *23*, 101468.

835 Cong, D., Ren, J., Zhou, Y., Wang, S., Liang, J., Ding, M., and Feng, W. (2021). Motor domain-mediated autoinhibition
836 dictates axonal transport by the kinesin UNC-104/KIF1A. PLoS Genet *17*, e1009940.

837 Consortium, C.e.D.M. (2012). large-scale screening for targeted knockouts in the Caenorhabditis elegans genome. G3
838 (Bethesda) *2*, 1415-1425.

839 Costa-Rodrigues, C., Couceiro, J., and Moreno, E. (2021). Cell competition from development to neurodegeneration. Dis
840 Model Mech *14*.

841 Cousin, M.A., and Robinson, P.J. (2001). The dephosphins: dephosphorylation by calcineurin triggers synaptic vesicle
842 endocytosis. Trends Neurosci *24*, 659-665.

843 Cuentas-Condori, A., Chen, S., Krout, M., Gallik, K.L., Tipps, J., Gailey, C., Flautt, L., Kim, H., Mulcahy, B., Zhen, M.,
844 *et al.* (2023). The epithelial Na(+) channel UNC-8 promotes an endocytic mechanism that recycles presynaptic components
845 to new boutons in remodeling neurons. Cell reports *42*, 113327.

846 Dai, Y., Taru, H., Deken, S.L., Grill, B., Ackley, B., Nonet, M.L., and Jin, Y. (2006). SYD-2 Liprin-alpha organizes
847 presynaptic active zone formation through ELKS. Nat Neurosci *9*, 1479-1487.

848 Dittman, J.S., and Kaplan, J.M. (2006). Factors regulating the abundance and localization of synaptobrevin in the plasma
849 membrane. Proc Natl Acad Sci U S A *103*, 11399-11404.

850 Duncan, A.L., Song, W., and Sansom, M.S.P. (2020). Lipid-Dependent Regulation of Ion Channels and G Protein-Coupled
851 Receptors: Insights from Structures and Simulations. Annu Rev Pharmacol Toxicol *60*, 31-50.

852 Eberhardt, J., Santos-Martins, D., Tillack, A.F., and Forli, S. (2021). AutoDock Vina 1.2.0: New Docking Methods,
853 Expanded Force Field, and Python Bindings. J Chem Inf Model *61*, 3891-3898.

854 Edelstein, A.D., Tsuchida, M.A., Amodaj, N., Pinkard, H., Vale, R.D., and Stuurman, N. (2014). Advanced methods of
855 microscope control using muManager software. J Biol Methods *1*.

856 Evans, R., O'Neill, M., Pritzel, A., Antropova, N., Senior, A., Green, T., Žídek, A., Bates, R., Blackwell, S., Yim, J.*, et al.*
857 (2022). Protein complex prediction with AlphaFold-Multimer. bioRxiv, 2021.2010.2004.463034.

858 Fares, H., and Grant, B. (2002). Deciphering endocytosis in Caenorhabditis elegans. Traffic *3*, 11-19.

859 Fares, H., and Greenwald, I. (2001). Genetic analysis of endocytosis in Caenorhabditis elegans: coelomocyte uptake
860 defective mutants. Genetics *159*, 133-145.

861 Filoteo, A.G., Enyedi, A., and Penniston, J.T. (1992). The lipid-binding peptide from the plasma membrane Ca2+ pump
862 binds calmodulin, and the primary calmodulin-binding domain interacts with lipid. J Biol Chem *267*, 11800-11805.

863 Fire, A. (1986). Integrative transformation of Caenorhabditis elegans. EMBO J *5*, 2673-2680.

Fleming, J.T., Squire, M.D., Barnes, T.M., Tornoe, C., Matsuda, K., Ahnn, J., Fire, A., Sulston, J.E., Barnard, E.A., Sattelle, D.B., *et al.* (1997). Caenorhabditis elegans levamisole resistance genes lev-1, unc-29, and unc-38 encode functional nicotinic acetylcholine receptor subunits. J Neurosci *17*, 5843-5857.

Gally, C., and Bessereau, J.L. (2003). GABA is dispensable for the formation of junctional GABA receptor clusters in Caenorhabditis elegans. J Neurosci *23*, 2591-2599.

Gan, Q., and Watanabe, S. (2018). Synaptic Vesicle Endocytosis in Different Model Systems. Front Cell Neurosci *12*, 171.

Gottschalk, A., Almedom, R.B., Schedletzky, T., Anderson, S.D., Yates, J.R., 3rd, and Schafer, W.R. (2005). Identification and characterization of novel nicotinic receptor-associated proteins in Caenorhabditis elegans. EMBO J *24*, 2566-2578.

Gross, O.P., and von Gersdorff, H. (2016). Recycling at synapses. eLife *5*.

Hall, D.H., and Hedgecock, E.M. (1991). Kinesin-related gene unc-104 is required for axonal transport of synaptic vesicles in C. elegans. Cell *65*, 837-847.

Hallgren, J., Tsirigos, K.D., Pedersen, M.D., Almagro Armenteros, J.J., Marcatili, P., Nielsen, H., Krogh, A., and Winther, O. (2022). DeepTMHMM predicts alpha and beta transmembrane proteins using deep neural networks. bioRxiv, 2022.2004.2008.487609.

Hansen, S.B., Tao, X., and MacKinnon, R. (2011). Structural basis of PIP2 activation of the classical inward rectifier K+ channel Kir2.2. Nature *477*, 495-498.

Haucke, V., Neher, E., and Sigrist, S.J. (2011). Protein scaffolds in the coupling of synaptic exocytosis and endocytosis. Nat Rev Neurosci *12*, 127-138.

Hoenderop, J.G., Voets, T., Hoefs, S., Weidema, F., Prenen, J., Nilius, B., and Bindels, R.J. (2003). Homo- and heterotetrameric architecture of the epithelial Ca2+ channels TRPV5 and TRPV6. EMBO J *22*, 776-785.

Hu, C.D., Chinenov, Y., and Kerppola, T.K. (2002). Visualization of interactions among bZIP and Rel family proteins in living cells using bimolecular fluorescence complementation. Mol Cell *9*, 789-798.

Hu, Z., Hom, S., Kudze, T., Tong, X.-J., Choi, S., Aramuni, G., Zhang, W., and Kaplan, J.M. (2012). Neurexin and Neuroligin Mediate Retrograde Synaptic Inhibition in *C. elegans*. Science *337*, 980-984.

Janosi, B., Liewald, J.F., Seidenthal, M., Yu, S.C., Umbach, S., Redzovic, J., Rentsch, D., Alcantara, I.C., Bergs, A.C.F., Schneider, M.W., *et al.* (2024). RIM and RIM-Binding Protein Localize Synaptic CaV2 Channels to Differentially Regulate Transmission in Neuronal Circuits. J Neurosci *44*.

Katan, M., and Cockcroft, S. (2020). Phosphatidylinositol(4,5)bisphosphate: diverse functions at the plasma membrane. Essays Biochem *64*, 513-531.

Kittelmann, M., Hegermann, J., Goncharov, A., Taru, H., Ellisman, M.H., Richmond, J.E., Jin, Y., and Eimer, S. (2013a). Liprin-alpha/SYD-2 determines the size of dense projections in presynaptic active zones in C. elegans. J Cell Biol *203*, 849-863.

Kittelmann, M., Liewald, J.F., Hegermann, J., Schultheis, C., Brauner, M., Steuer Costa, W., Wabnig, S., Eimer, S., and Gottschalk, A. (2013b). In vivo synaptic recovery following optogenetic hyperstimulation. Proc Natl Acad Sci U S A *110*, E3007-3016.

Klopfenstein, D.R., and Vale, R.D. (2004). The lipid binding pleckstrin homology domain in UNC-104 kinesin is necessary for synaptic vesicle transport in Caenorhabditis elegans. Mol Biol Cell *15*, 3729-3739.

Kononenko, N.L., and Haucke, V. (2015). Molecular mechanisms of presynaptic membrane retrieval and synaptic vesicle reformation. Neuron *85*, 484-496.

Kraev, A., Kraev, N., and Carafoli, E. (1999). Identification and functional expression of the plasma membrane calcium ATPase gene family from Caenorhabditis elegans. J Biol Chem *274*, 4254-4258.

Krebs, J. (2022). Structure, Function and Regulation of the Plasma Membrane Calcium Pump in Health and Disease. Int J Mol Sci *23*.

Krick, N., Ryglewski, S., Pichler, A., Bikbaev, A., Gotz, T., Kobler, O., Heine, M., Thomas, U., and Duch, C. (2021). Separation of presynaptic Ca(v)2 and Ca(v)1 channel function in synaptic vesicle exo- and endocytosis by the membrane anchored Ca(2+) pump PMCA. Proc Natl Acad Sci U S A *118*, e2106621118.

Kumashiro, S., Lu, Y.F., Tomizawa, K., Matsushita, M., Wei, F.Y., and Matsui, H. (2005). Regulation of synaptic vesicle recycling by calcineurin in different vesicle pools. Neurosci Res *51*, 435-443.

Larkin, M.A., Blackshields, G., Brown, N.P., Chenna, R., McGettigan, P.A., McWilliam, H., Valentin, F., Wallace, I.M., Wilm, A., Lopez, R., *et al.* (2007). Clustal W and Clustal X version 2.0. Bioinformatics *23*, 2947-2948.

Leitz, J., and Kavalali, E.T. (2016). Ca2+ Dependence of Synaptic Vesicle Endocytosis. Neuroscientist *22*, 464-476.

Li, T.N., Chen, Y.J., Lu, T.Y., Wang, Y.T., Lin, H.C., and Yao, C.K. (2020). A positive feedback loop between Flower and PI(4,5)P(2) at periactive zones controls bulk endocytosis in Drosophila. eLife *9*.

Liewald, J.F., Brauner, M., Stephens, G.J., Bouhours, M., Schultheis, C., Zhen, M., and Gottschalk, A. (2008). Optogenetic analysis of synaptic function. Nat Methods *5*, 895-902.

Liu, Q., Chen, B., Yankova, M., Morest, D.K., Maryon, E., Hand, A.R., Nonet, M.L., and Wang, Z.W. (2005). Presynaptic ryanodine receptors are required for normal quantal size at the Caenorhabditis elegans neuromuscular junction. J Neurosci *25*, 6745-6754.

Lopreiato, R., Giacomello, M., and Carafoli, E. (2014a). The plasma membrane calcium pump: new ways to look at an old enzyme. J Biol Chem *289*, 10261-10268.

Lou, X. (2018). Sensing Exocytosis and Triggering Endocytosis at Synapses: Synaptic Vesicle Exocytosis-Endocytosis Coupling. Front Cell Neurosci *12*, 66.

Lu, Y., Ahamed, T., Mulcahy, B., Meng, J., Witvliet, D., Guan, S.A., Holmyard, D., Hung, W., Wen, Q., Chisholm, A.D., *et al.* (2022). Extrasynaptic signaling enables an asymmetric juvenile motor circuit to produce symmetric undulation. Curr Biol *32*, 4631-4644 e4635.

Madan, E., Pelham, C.J., Nagane, M., Parker, T.M., Canas-Marques, R., Fazio, K., Shaik, K., Yuan, Y., Henriques, V., Galzerano, A., *et al.* (2019). Flower isoforms promote competitive growth in cancer. Nature *572*, 260-264.

Mahoney, T.R., Luo, S., and Nonet, M.L. (2006). Analysis of synaptic transmission in Caenorhabditis elegans using an aldicarb-sensitivity assay. Nat Protoc *1*, 1772-1777.

Mantilla, G., Perez-Gordones, M.C., Cisneros-Montufar, S., Benaim, G., Navarro, J.C., Mendoza, M., and Ramirez-Iglesias, J.R. (2023). Structural Analysis and Diversity of Calmodulin-Binding Domains in Membrane and Intracellular Ca(2+)-ATPases. J Membr Biol *256*, 159-174.

McGilvray, P.T., Anghel, S.A., Sundaram, A., Zhong, F., Trnka, M.J., Fuller, J.R., Hu, H., Burlingame, A.L., and Keenan, R.J. (2020). An ER translocon for multi-pass membrane protein biogenesis. eLife *9*, e56889.

Miller-Fleming, T.W., Petersen, S.C., Manning, L., Matthewman, C., Gornet, M., Beers, A., Hori, S., Mitani, S., Bianchi, L., Richmond, J., *et al.* (2016). The DEG/ENaC cation channel protein UNC-8 drives activity-dependent synapse removal in remodeling GABAergic neurons. eLife *5*.

Nagel, G., Brauner, M., Liewald, J.F., Adeishvili, N., Bamberg, E., and Gottschalk, A. (2005). Light activation of channelrhodopsin-2 in excitable cells of Caenorhabditis elegans triggers rapid behavioral responses. Curr Biol *15*, 2279-2284.

Nakai, J., Ohkura, M., and Imoto, K. (2001). A high signal-to-noise Ca(2+) probe composed of a single green fluorescent protein. Nat Biotechnol *19*, 137-141.

Nonet, M.L. (1999). Visualization of synaptic specializations in live C. elegans with synaptic vesicle protein-GFP fusions. J Neurosci Methods *89*, 33-40.

Nussbaum-Krammer, C.I., Neto, M.F., Brielmann, R.M., Pedersen, J.S., and Morimoto, R.I. (2015). Investigating the spreading and toxicity of prion-like proteins using the metazoan model organism C. elegans. Journal of visualized experiments : JoVE, 52321.

Oda, K., Vierock, J., Oishi, S., Rodriguez-Rozada, S., Taniguchi, R., Yamashita, K., Wiegert, J.S., Nishizawa, T., Hegemann, P., and Nureki, O. (2018). Crystal structure of the red light-activated channelrhodopsin Chrimson. Nature communications *9*, 3949.

Okamoto, Y., Lipstein, N., Hua, Y., Lin, K.H., Brose, N., Sakaba, T., and Midorikawa, M. (2016). Distinct modes of endocytotic presynaptic membrane and protein uptake at the calyx of Held terminal of rats and mice. eLife *5*.

Ono, Y., Mori, Y., Egashira, Y., Sumiyama, K., and Takamori, S. (2019). Expression of plasma membrane calcium ATPases confers Ca(2+)/H(+) exchange in rodent synaptic vesicles. Scientific reports *9*, 4289.

958 Penniston, J.T., Padanyi, R., Paszty, K., Varga, K., Hegedus, L., and Enyedi, A. (2014). Apart from its known function, the
959 plasma membrane Ca(2)(+)ATPase can regulate Ca(2)(+) signaling by controlling phosphatidylinositol 4,5-bisphosphate
960 levels. J Cell Sci *127*, 72-84.

961 Petrova, E., Lopez-Gay, J.M., Rhiner, C., and Moreno, E. (2012). Flower-deficient mice have reduced susceptibility to skin
962 papilloma formation. Dis Model Mech *5*, 553-561.

963 Posor, Y., Eichhorn-Grunig, M., and Haucke, V. (2015). Phosphoinositides in endocytosis. Biochim Biophys Acta *1851*,
964 794-804.

965 Rhiner, C., Lopez-Gay, J.M., Soldini, D., Casas-Tinto, S., Martin, F.A., Lombardia, L., and Moreno, E. (2010). Flower
966 forms an extracellular code that reveals the fitness of a cell to its neighbors in Drosophila. Dev Cell *18*, 985-998.

967 Ribalet, B., John, S.A., Xie, L.H., and Weiss, J.N. (2005). Regulation of the ATP-sensitive K channel Kir6.2 by ATP and
968 PIP(2). Journal of molecular and cellular cardiology *39*, 71-77.

969 Richmond, J.E., and Jorgensen, E.M. (1999). One GABA and two acetylcholine receptors function at the C. elegans
970 neuromuscular junction. Nat Neurosci *2*, 791-797.

971 Rizzoli, S.O. (2014). Synaptic vesicle recycling: steps and principles. EMBO J *33*, 788-822.

972 Rohacs, T. (2024). Phosphoinositide Regulation of TRP Channels: A Functional Overview in the Structural Era. Annu Rev
973 Physiol *86*, 329-355.

974 Rosignoli, S., and Paiardini, A. (2022). DockingPie: a consensus docking plugin for PyMOL. Bioinformatics *38*, 4233-
975 4234.

976 Rudd, J.C., Maity, S., Grunkemeyer, J.A., Snyder, J.C., Lovas, S., and Hansen, L.A. (2023). Membrane structure and
977 internalization dynamics of human Flower isoforms hFWE3 and hFWE4 indicate a conserved endocytic role for hFWE4.
978 J Biol Chem *299*, 104945.

979 Saheki, Y., and De Camilli, P. (2012). Synaptic vesicle endocytosis. Cold Spring Harb Perspect Biol *4*, a005645.

980 Salcini, A.E., Hilliard, M.A., Croce, A., Arbucci, S., Luzzi, P., Tacchetti, C., Daniell, L., De Camilli, P., Pelicci, P.G., Di
981 Fiore, P.P., *et al.* (2001). The Eps15 C. elegans homologue EHS-1 is implicated in synaptic vesicle recycling. Nat Cell Biol
982 *3*, 755-760.

983 Sankaranarayanan, S., De Angelis, D., Rothman, J.E., and Ryan, T.A. (2000). The use of pHluorins for optical
984 measurements of presynaptic activity. Biophys J *79*, 2199-2208.

985 Sattelle, D.B., Culetto, E., Grauso, M., Raymond, V., Franks, C.J., and Towers, P. (2002). Functional genomics of
986 ionotropic acetylcholine receptors in Caenorhabditis elegans and Drosophila melanogaster. Novartis Found Symp *245*, 240-
987 257; discussion 257-260, 261-244.

988 Schultheis, C., Brauner, M., Liewald, J.F., and Gottschalk, A. (2011). Optogenetic analysis of GABAB receptor signaling
989 in Caenorhabditis elegans motor neurons. J Neurophysiol *106*, 817-827.

990 Schuske, K.R., Richmond, J.E., Matthies, D.S., Davis, W.S., Runz, S., Rube, D.A., van der Bliek, A.M., and Jorgensen,
991 E.M. (2003). Endophilin is required for synaptic vesicle endocytosis by localizing synaptojanin. Neuron *40*, 749-762.

992 Seidenthal, M., Janosi, B., Rosenkranz, N., Schuh, N., Elvers, N., Willoughby, M., Zhao, X., and Gottschalk, A. (2023).
993 pOpsicle: An all-optical reporter system for synaptic vesicle recycling combining pH-sensitive fluorescent proteins with
994 optogenetic manipulation of neuronal activity. Front Cell Neurosci *17*, 1120651.

995 Seidenthal, M., Vettkotter, D., and Gottschalk, A. (2022). WormRuler: A software to track body length used to characterize
996 a super red-shifted channelrhodopsin in Caenorhabditis elegans. MicroPubl Biol *2022*.

997 Simon, D.J., Madison, J.M., Conery, A.L., Thompson-Peer, K.L., Soskis, M., Ruvkun, G.B., Kaplan, J.M., and Kim, J.K.
998 (2008). The MicroRNA miR-1 Regulates a MEF-2-Dependent Retrograde Signal at Neuromuscular Junctions. Cell *133*,
999 903-915.

1000 Smalinskaitė, L., Kim, M.K., Lewis, A.J.O., Keenan, R.J., and Hegde, R.S. (2022). Mechanism of an intramembrane
1001 chaperone for multipass membrane proteins. Nature *611*, 161-166.

1002 Stauffer, T.P., Ahn, S., and Meyer, T. (1998). Receptor-induced transient reduction in plasma membrane PtdIns(4,5)P2
1003 concentration monitored in living cells. Curr Biol *8*, 343-346.

1004 Swierczek, N.A., Giles, A.C., Rankin, C.H., and Kerr, R.A. (2011). High-throughput behavioral analysis in C. elegans. Nat
1005 Methods *8*, 592-598.

1006 Takamori, S., Holt, M., Stenius, K., Lemke, E.A., Gronborg, M., Riedel, D., Urlaub, H., Schenck, S., Brugger, B., Ringler,
1007 P., *et al.* (2006). Molecular anatomy of a trafficking organelle. Cell *127*, 831-846.

1008 Taylor, S.R., Santpere, G., Weinreb, A., Barrett, A., Reilly, M.B., Xu, C., Varol, E., Oikonomou, P., Glenwinkel, L.,
1009 McWhirter, R., *et al.* (2021). Molecular topography of an entire nervous system. Cell *184*, 4329-4347 e4323.

1010 Tong, X.J., Lopez-Soto, E.J., Li, L., Liu, H., Nedelcu, D., Lipscombe, D., Hu, Z., and Kaplan, J.M. (2017). Retrograde
1011 Synaptic Inhibition Is Mediated by alpha-Neurexin Binding to the alpha2delta Subunits of N-Type Calcium Channels.
1012 Neuron *95*, 326-340 e325.

1013 Vashlishan, A.B., Madison, J.M., Dybbs, M., Bai, J., Sieburth, D., Ch'ng, Q., Tavazoie, M., and Kaplan, J.M. (2008). An
1014 RNAi screen identifies genes that regulate GABA synapses. Neuron *58*, 346-361.

1015 Vettkotter, D., Schneider, M., Goulden, B.D., Dill, H., Liewald, J., Zeiler, S., Guldan, J., Ates, Y.A., Watanabe, S., and
1016 Gottschalk, A. (2022). Rapid and reversible optogenetic silencing of synaptic transmission by clustering of synaptic
1017 vesicles. Nature communications *13*, 7827.

1018 Ward, S., Thomson, N., White, J.G., and Brenner, S. (1975). Electron microscopical reconstruction of the anterior sensory
1019 anatomy of the nematode Caenorhabditis elegans. J Comp Neurol *160*, 313-337.

1020 Watanabe, S., Davis, M.W., Kusick, G.F., Iwasa, J., and Jorgensen, E.M. (2020). SynapsEM: Computer-Assisted Synapse
1021 Morphometry. Front Synaptic Neurosci *12*, 584549.

1022 Watanabe, S., Liu, Q., Davis, M.W., Hollopeter, G., Thomas, N., Jorgensen, N.B., and Jorgensen, E.M. (2013). Ultrafast
1023 endocytosis at Caenorhabditis elegans neuromuscular junctions. eLife *2*, e00723.

1024 Watanabe, S., Trimbuch, T., Camacho-Perez, M., Rost, B.R., Brokowski, B., Sohl-Kielczynski, B., Felies, A., Davis, M.W.,
1025 Rosenmund, C., and Jorgensen, E.M. (2014). Clathrin regenerates synaptic vesicles from endosomes. Nature *515*, 228-233.

1026 Weimer, R.M. (2006). Preservation of C. elegans tissue via high-pressure freezing and freeze-substitution for ultrastructural
1027 analysis and immunocytochemistry. Methods Mol Biol *351*, 203-221.

1028 Weissenberger, S., Schultheis, C., Liewald, J.F., Erbguth, K., Nagel, G., and Gottschalk, A. (2011). PACalpha--an
1029 optogenetic tool for in vivo manipulation of cellular cAMP levels, neurotransmitter release, and behavior in Caenorhabditis
1030 elegans. J Neurochem *116*, 616-625.

1031 Wu, L.G., and Betz, W.J. (1998). Kinetics of synaptic depression and vesicle recycling after tetanic stimulation of frog
1032 motor nerve terminals. Biophys J *74*, 3003-3009.

1033 Wu, X.S., McNeil, B.D., Xu, J., Fan, J., Xue, L., Melicoff, E., Adachi, R., Bai, L., and Wu, L.G. (2009). Ca(2+) and
1034 calmodulin initiate all forms of endocytosis during depolarization at a nerve terminal. Nat Neurosci *12*, 1003-1010.

1035 Wu, Y., O'Toole, E.T., Girard, M., Ritter, B., Messa, M., Liu, X., McPherson, P.S., Ferguson, S.M., and De Camilli, P.
1036 (2014). A dynamin 1-, dynamin 3- and clathrin-independent pathway of synaptic vesicle recycling mediated by bulk
1037 endocytosis. eLife *3*, e01621.

1038 Xue, L., Zhang, Z., McNeil, B.D., Luo, F., Wu, X.S., Sheng, J., Shin, W., and Wu, L.G. (2012). Voltage-dependent calcium
1039 channels at the plasma membrane, but not vesicular channels, couple exocytosis to endocytosis. Cell reports *1*, 632-638.

1040 Yamashita, T. (2012). Ca2+-dependent regulation of synaptic vesicle endocytosis. Neurosci Res *73*, 1-7.

1041 Yao, C.K., Lin, Y.Q., Ly, C.V., Ohyama, T., Haueter, C.M., Moiseenkova-Bell, V.Y., Wensel, T.G., and Bellen, H.J.
1042 (2009). A synaptic vesicle-associated Ca2+ channel promotes endocytosis and couples exocytosis to endocytosis. Cell *138*,
1043 947-960.

1044 Yao, C.K., Liu, Y.T., Lee, I.C., Wang, Y.T., and Wu, P.Y. (2017). A Ca2+ channel differentially regulates Clathrin-
1045 mediated and activity-dependent bulk endocytosis. PLoS Biol *15*, e2000931.

1046 Yu, S.C., Janosi, B., Liewald, J.F., Wabnig, S., and Gottschalk, A. (2018). Endophilin A and B Join Forces With Clathrin
1047 to Mediate Synaptic Vesicle Recycling in Caenorhabditis elegans. Frontiers in molecular neuroscience *11*, 196.

1048 Zhang, M., Ma, Y., Ye, X., Zhang, N., Pan, L., and Wang, B. (2023). TRP (transient receptor potential) ion channel family:
1049 structures, biological functions and therapeutic interventions for diseases. Signal Transduct Target Ther *8*, 261.

1050

FIGURES

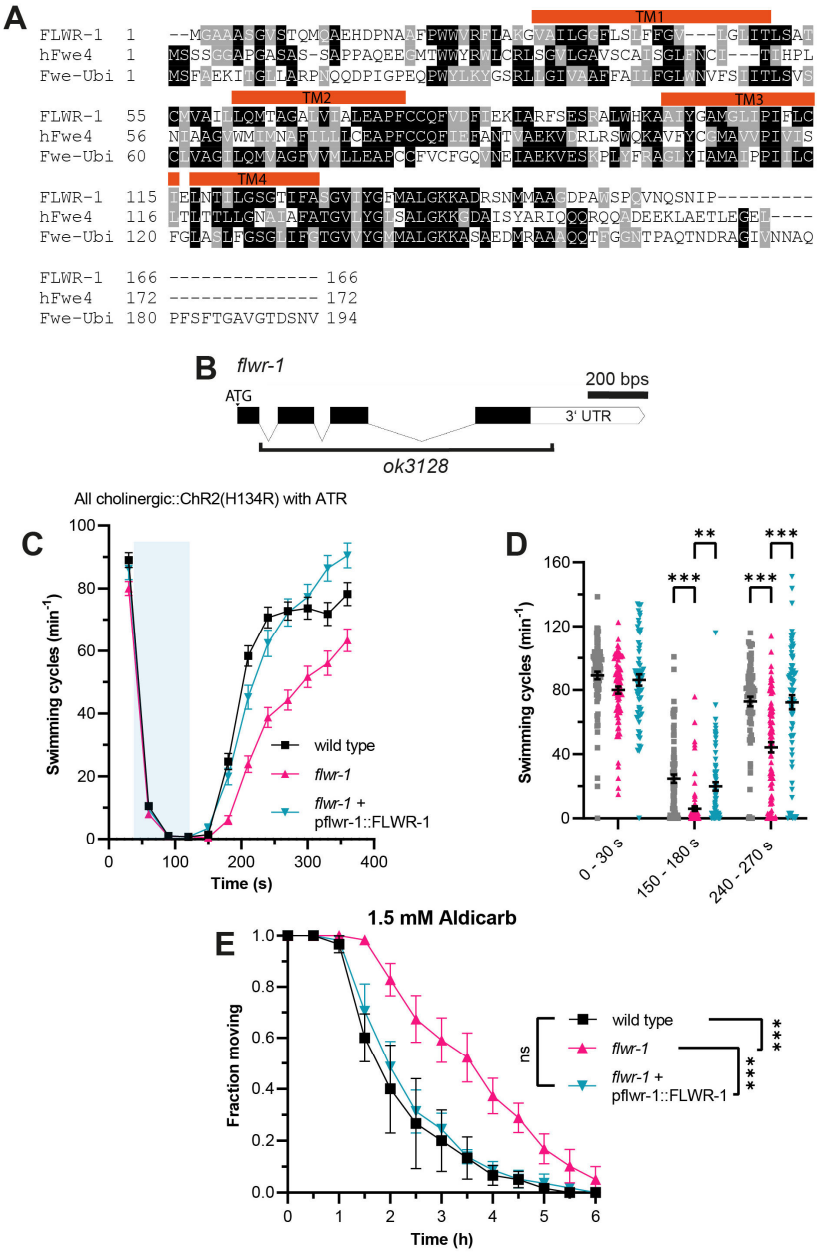

FIGURES

Fig. 1. Loss of FLWR-1 induces defects in neurotransmission following intense stimulation.

(A) Alignment of the amino acid sequences of FLWR-1 to hFwe4 (*Homo sapiens*) and Fwe-Ubi/FweA (*Drosophila melanogaster*). Shading depicts evolutionary conservation of amino acid residues (identity – black; homology – grey). Position of TM helices indicated in red refers to the FLWR-1 sequence. **(B)** Schematic representation of the *flwr-1*/F20D1.1 gene locus and the size of the *ok3128* deletion. Bars represent exons and connecting lines introns. **(C)** Mean (± SEM) swimming cycles of animals expressing ChR2(H134R) in cholinergic motor neurons (*unc-17* promoter). All animals were treated with ATR. A 90 s light pulse (470 nm, 1 mW/mm^2) was applied after 30 s as indicated by the blue shade. Number of animals accumulated from N = 3 biological replicates: wild type = 80 – 88, *flwr-1* = 80 – 91, FLWR-1 rescue = 62 – 75. **(D)** Statistical analysis of swimming speed at different time points as depicted in (C). Mean (± SEM). Each dot represents a single animal. Mixed-effects model analysis with Tukey's correction. Only statistically significant differences are depicted. **p < 0.01, *** p < 0.001. **(E)** Mean (± SEM) fraction of moving animals after exposure to 1.5 mM aldicarb. N = 4 biological replicates. Two-way ANOVA with Tukey's correction. ns not significant p > 0.05, *** p < 0.001.

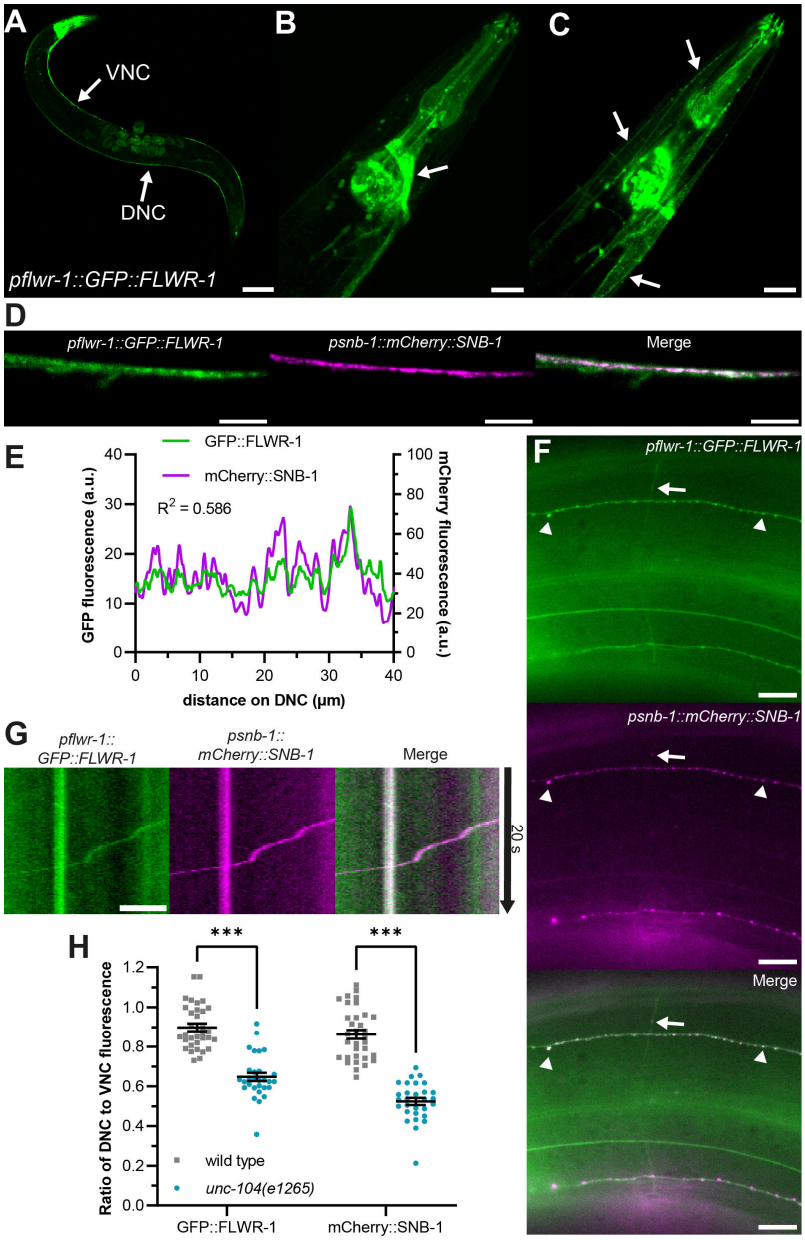

Fig. 2. FLWR-1 is expressed in neurons and localizes to synaptic vesicles and the plasma membrane.

(A - D) Confocal micrographs (maximum projection of z-stacks or single plane) of animals co-expressing *flwr-1p::GFP::FLWR-1* and *psnb-1::mCherry::SNB-1*. **(A)** Overview of GFP::FLWR-1 expression. Arrows indicate dorsal and ventral nerve cords (DNC and VNC, respectively). Scale bar, 100 µm. **(B)** GFP::FLWR-1 in head neurons and pharynx. Scale bar, 20 µm. **(C)** Animal depicted in (B), single plane showing neck muscle cells. Arrows indicate GFP::FLWR-1 localization to the plasma membrane. Scale bar, 20 µm. **(D)** GFP and mCherry fluorescence in the DNC. Scale bar, 10 µm. **(E)** Line scan analysis of colocalization of GFP::FLWR-1 and mCherry::SNB-1 along the DNC as represented in (D). R^2 as determined by Pearson correlation. a.u. = arbitrary units of fluorescence intensity. **(F)** Micrograph depicting GFP::FLWR-1 and mCherry::SNB-1 fluorescence in sublateral nerve cords and commissures. Arrowheads indicate synaptic puncta. Arrow points towards SV precursor travelling along commissure as shown in Supplementary Movie 1. Scale bar, 10 µm. **(G)** Kymograph representing the SV precursor indicated in (F) travelling along commissures. Scale bar, 2 µm. **(H)** Comparison of the ratio of DNC to VNC fluorescence of GFP::FLWR-1 and mCherry::SNB-1 in wild type and *unc-104(e1265)* mutant background. Mean (± SEM). Each dot represents a single animal. Two-way ANOVA with Šídák's correction. *** $p < 0.001$. Number of animals imaged in N = 3 biological replicates: wild type = 33, *unc-104* = 29.

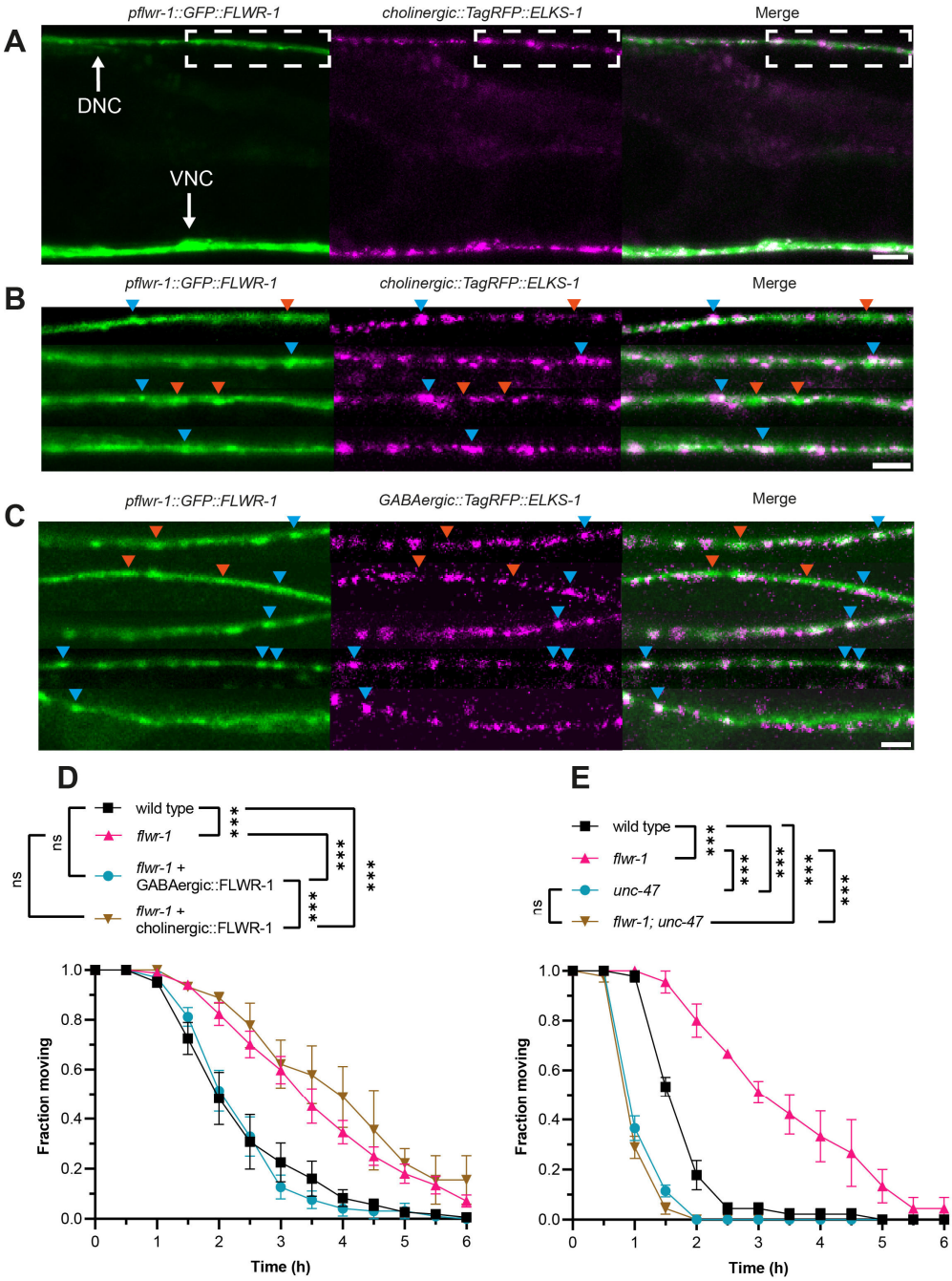

Fig. 3. GABAergic signaling is increased in *flwr-1* knockout mutants.

(**A**) Representative confocal micrographs of an animal co-expressing *flwr-1p::GFP::FLWR-1* and *TagRFP::ELKS-1* in cholinergic motor neurons (*unc-17(short)* promoter). The region in the DNC used to acquire images shown in **B** and **C** is indicated; this position is posterior to the vulva, anterior is left. Scale bar, 10 µm. **(B, C)** DNCs in animals co-expressing *flwr-1p::GFP::FLWR-1* and *TagRFP::ELKS-1* in cholinergic motor neurons (*unc-17(short)* promoter), or in GABAergic neurons (*unc-47* promoter; C), respectively. Scale bar, 5 µm. Examples of fluorescent puncta which contain either both, FLWR-1 and ELKS-1 (blue arrowheads), or FLWR-1 only (red arrowheads) are indicated. The same puncta are indicated in the respective analysis of signal density along the DNC in **Figure 3 – Figure supplement 1A, B**. **(D)** Mean (± SEM) fraction of moving animals after exposure to 1.5 mM aldicarb with cholinergic (*unc-17p*) and GABAergic (*unc-47p*) expression of FLWR-1 in *flwr-1(ok3128)* mutant background. N = 3 - 8 biological replicates. **(E)** Mean (± SEM) fraction of moving animals after exposure to 1.5 mM aldicarb with *unc-47(e307)* and *unc-47(e307)/flwr-1(ok3128)* double mutants. N = 3 biological replicates. Two-way ANOVA with Tukey's correction in D, E. ns not significant, *** $p < 0.001$.

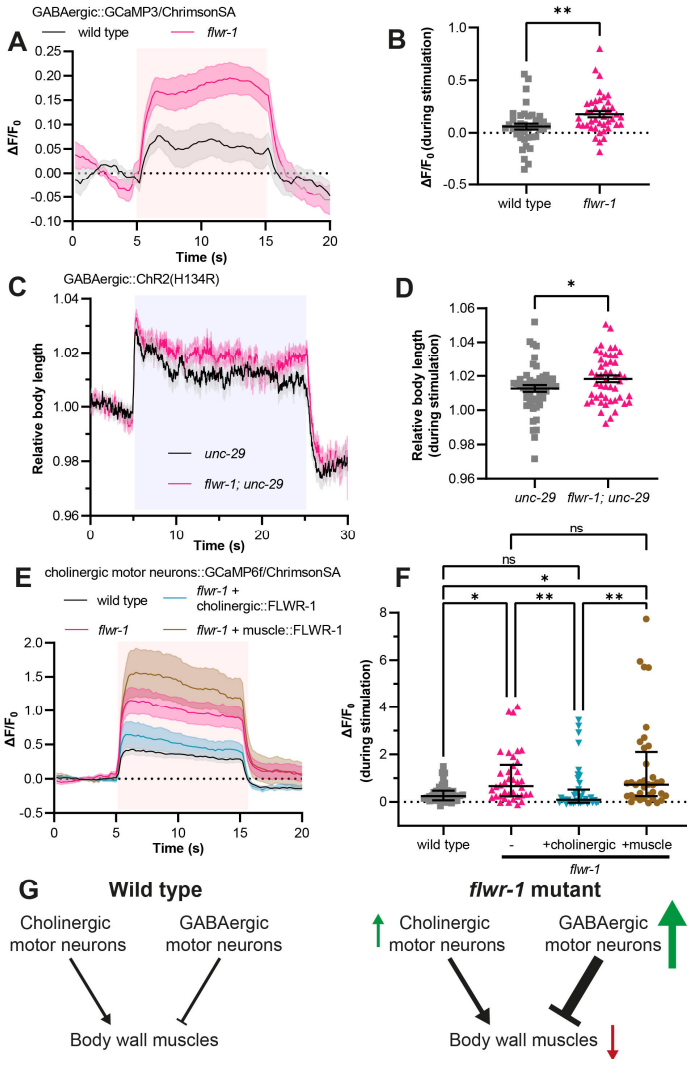

Fig. 4. Loss of FLWR-1 leads to increased Ca^{2+} levels during stimulation.

(**A**) Mean (± SEM) normalized fluorescence in synaptic puncta of the DNC of animals expressing GCaMP3 and ChrimsonSA in GABAergic neurons (*unc-25* promoter). All animals were supplemented with ATR. A 10 s light pulse (590 nm, 40 µW/mm^2) was applied after 5 s as indicated by the red shade. **(B)** Mean (± SEM) normalized fluorescence during stimulation (seconds 6 to 14) as depicted in (A). Each dot indicates a single animal. Unpaired t-test. ** $p < 0.01$. **(A + B)** Number of animals imaged in N = 5 biological replicates: wild type = 40, *flwr-1* = 41. Outliers were removed from both datasets as detected by the iterative Grubb's method (GraphPad Prism). **(C)** Mean (± SEM) body length of animals expressing ChR2(H134R) in GABAergic neurons (*unc-47* promoter) in the *unc-29(e1072)* mutant background, normalized to the average before stimulation. All animals were supplemented with ATR. A 20 s light pulse (470 nm, 100 µW/mm^2) was applied after 5 s as indicated by the blue shade. **(D)** Mean (± SEM) relative body length during stimulation (seconds 6 to 24) as depicted in (C). Each dot indicates a single animal. Unpaired t-test. * $p < 0.05$. Number of animals measured in N = 4 biological replicates: wild type = 51, *flwr-1* = 49. **(E)** Mean (± SEM) normalized fluorescence in synaptic puncta of the DNC of animals expressing GCaMP6f and ChrimsonSA in cholinergic motor neurons (*unc-17b* promoter). All animals were supplemented with ATR. A 10 s light pulse (590 nm, 40 µW/mm^2) was applied after 5 s as indicated by red shade. **(F)** Median (with IQR) normalized fluorescence during stimulation (seconds 6 to 14) as depicted in (E). Each dot indicates a single animal. Kruskal-Wallis test. Only statistically significant differences are depicted. * $p < 0.05$, ** $p < 0.01$. **(E + F)** Number of animals imaged in N = 5 biological replicates: wild type = 40, *flwr-1* = 38, cholinergic rescue = 39, muscle rescue = 36. No outliers were detected by the iterative Grubb's method. **(G)** Schematic representation of motor neuron innervation of BWMs. Arrows indicate the putatively increased (green) or decreased (red) neurotransmission/excitation of the involved cell types in *flwr-1* mutants compared to wildtype.

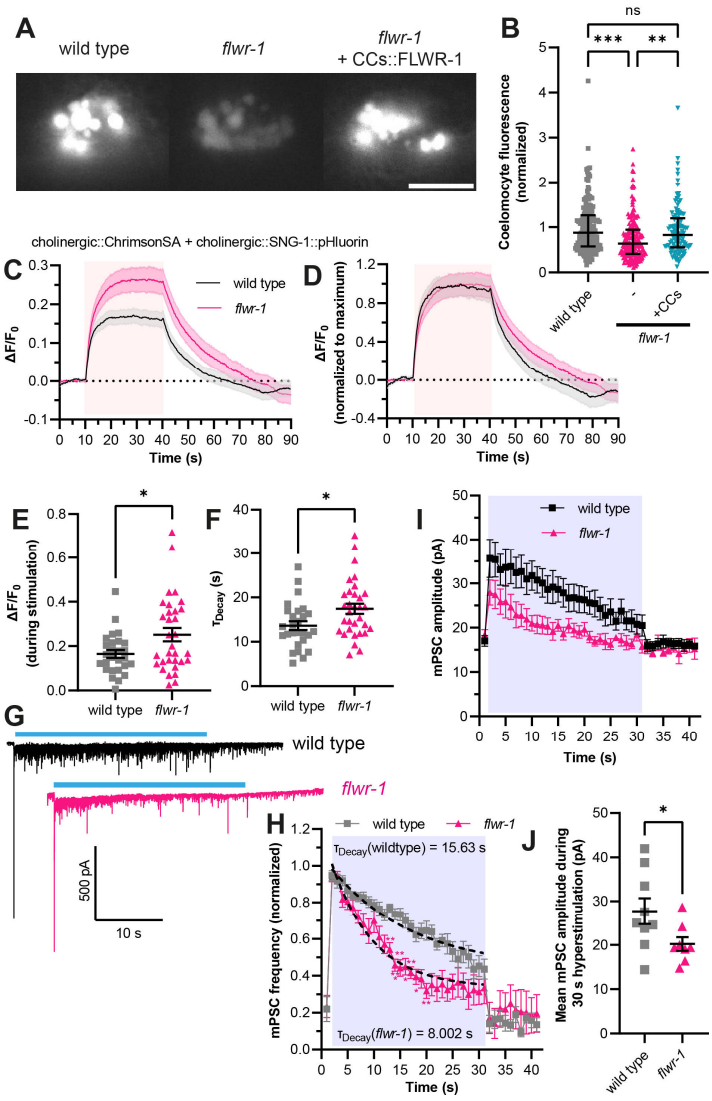

Fig. 5. FLWR-1 facilitates endocytosis in non-neuronal and neuronal cells.

(A) Exemplary images of the coelomocytes (CCs) in wild type, *flwr-1(ok3128)* and in *flwr-1* mutants expressing FLWR-1 in CCs (*unc-122* promoter). GFP containing a secretion signal sequence (ssGFP) was expressed in BWMs (*myo-3* promoter). Scale bar, 10 µm. **(B)** Median (with IQR) normalized fluorescence of CCs. Each dot indicates a single CC. Kruskal-Wallis test. ** $p < 0.001$*** $p < 0.001$. Number of CCs imaged in N = 3 biological replicates: wild type = 158, *flwr-1* = 185, rescue = 113. **(C)** Mean (± SEM) normalized DNC fluorescence of animals expressing SNG-1::pHluorin and ChrimsonSA in cholinergic neurons (*unc-17* promoter). All animals were supplemented with ATR. A 30 s light pulse (590 nm, 40 µW/mm^2) was applied after 10 s as indicated by the red shade. **(D)** Mean (± SEM) pHluorin fluorescence as depicted in (C) but additionally normalized to the maximum value of each dataset. **(E)** Mean (± SEM) normalized fluorescence during stimulation (seconds 15 to 35) as depicted in (C). Each dot indicates a single animal. Unpaired t-test. **(F)** Mean (± SEM) calculated exponential decay constants of fluorescence decline after stimulation. Each dot indicates a single animal. Unpaired t-test. **(C – F)** Number of animals imaged in N = 5 biological replicates: wild type = 27, *flwr-1* = 32. * $p < 0.05$. **(G)** Representative voltage-clamp recordings of currents in BWMs. Animals expressing ChR2(H134R) in cholinergic motor neurons (*unc-17* promoter, transgene *zxIs6*) were treated with ATR. A 30 s light stimulus (470 nm, 8 mW/mm^2) was applied as indicated by blue bars. **(H)** Normalized mPSC frequency in BWMs. All animals were treated with ATR. A 30 s light pulse (470 nm, 8 mW/mm^2) was applied as indicated by the blue shade. Dashed lines indicate one-phase exponential regression analysis fitted to the mean mPSC frequencies during stimulation. Calculated time constants of decay are shown. Two-way ANOVA with Šidák's correction. All significant differences to wild type are depicted. **(I)** mPSC amplitude in BWMs of animals measured in (G + H). **(J)** Mean (± SEM) mPSC amplitude during light stimulation as indicated in (I). Unpaired t-test. * $p < 0.05$. (G - J) Number of animals: wild type = 9, *flwr-1* = 8.

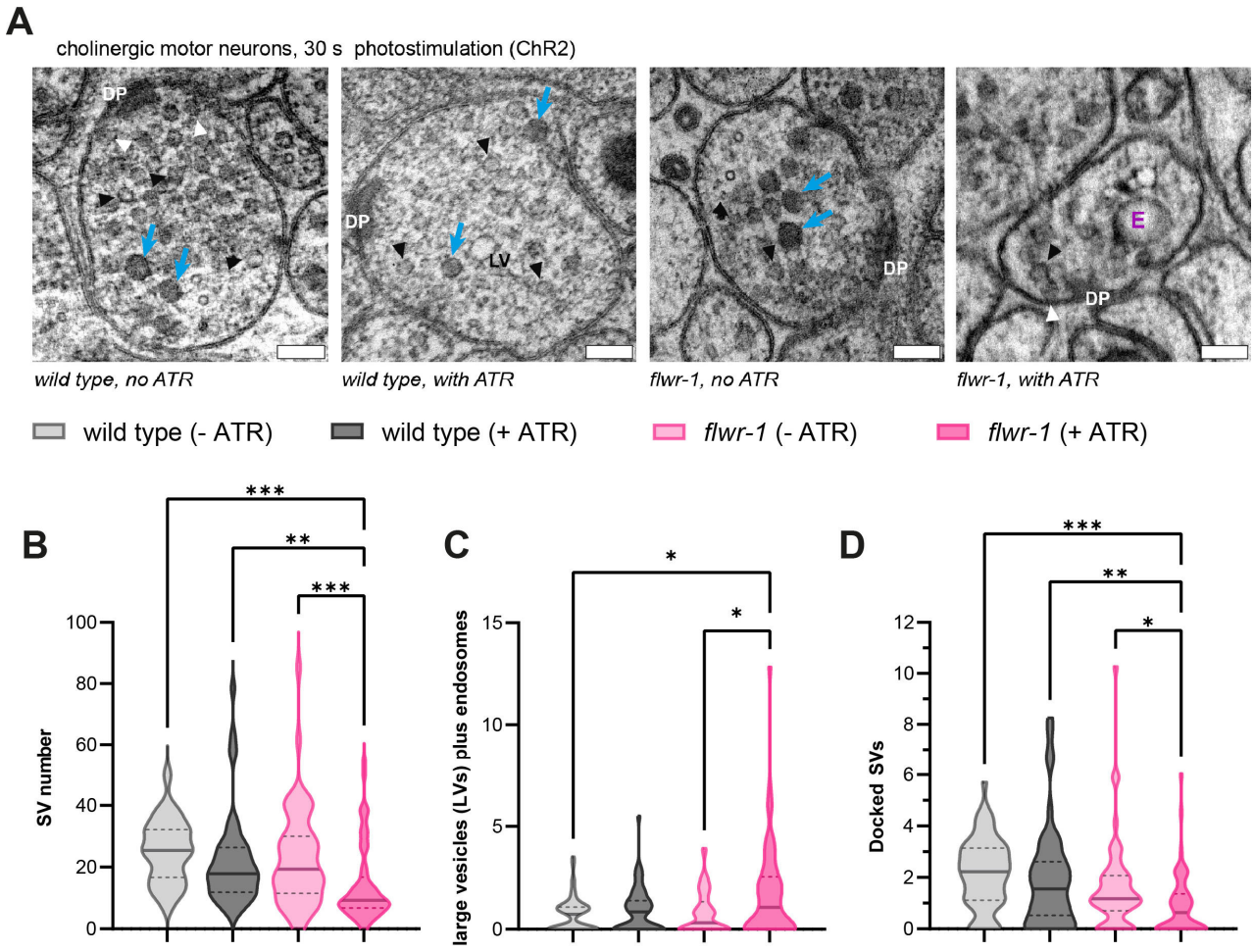

Fig. 6. Ultra-structural analysis reveals defective recycling of SVs after stimulation in *flwr-1* mutants.

(A) Representative TEM micrographs of cholinergic *en-passant* synapses in wild type and *flwr-1(ok3128)* animals expressing ChR2(H134R) in cholinergic neurons (*unc-17* promoter). Animals were optionally treated with ATR as indicated. Dense projections (DP), endosomes (E), dense core vesicles (blue arrows), SVs (black arrowheads), docked vesicles (white arrowheads) and large vesicles (LV) are indicated. Scale bars, 100 nm. **(B)** Violin plot depicting the number of SVs counted per synaptic profile. **(C)** Violin plot depicting the number of large endcytic vesicels and 'endosomes' per synapse. **(D)** Violin plot depicting the number of docked vesicles observed per synaptic profile. **(B - D)** Bold line represents the median, and the dashed lines the IQR. Kruskal-Wallis test. Only statistically significant differences are depicted. * $p < 0.05$,** $p < 0.01$, *** $p < 0.001$. Number of synaptic profiles imaged: wild type (-ATR) = 56, wild type (-ATR) = 51, *flwr-1* (-ATR) = 55, *flwr-1* (+ATR) = 59.

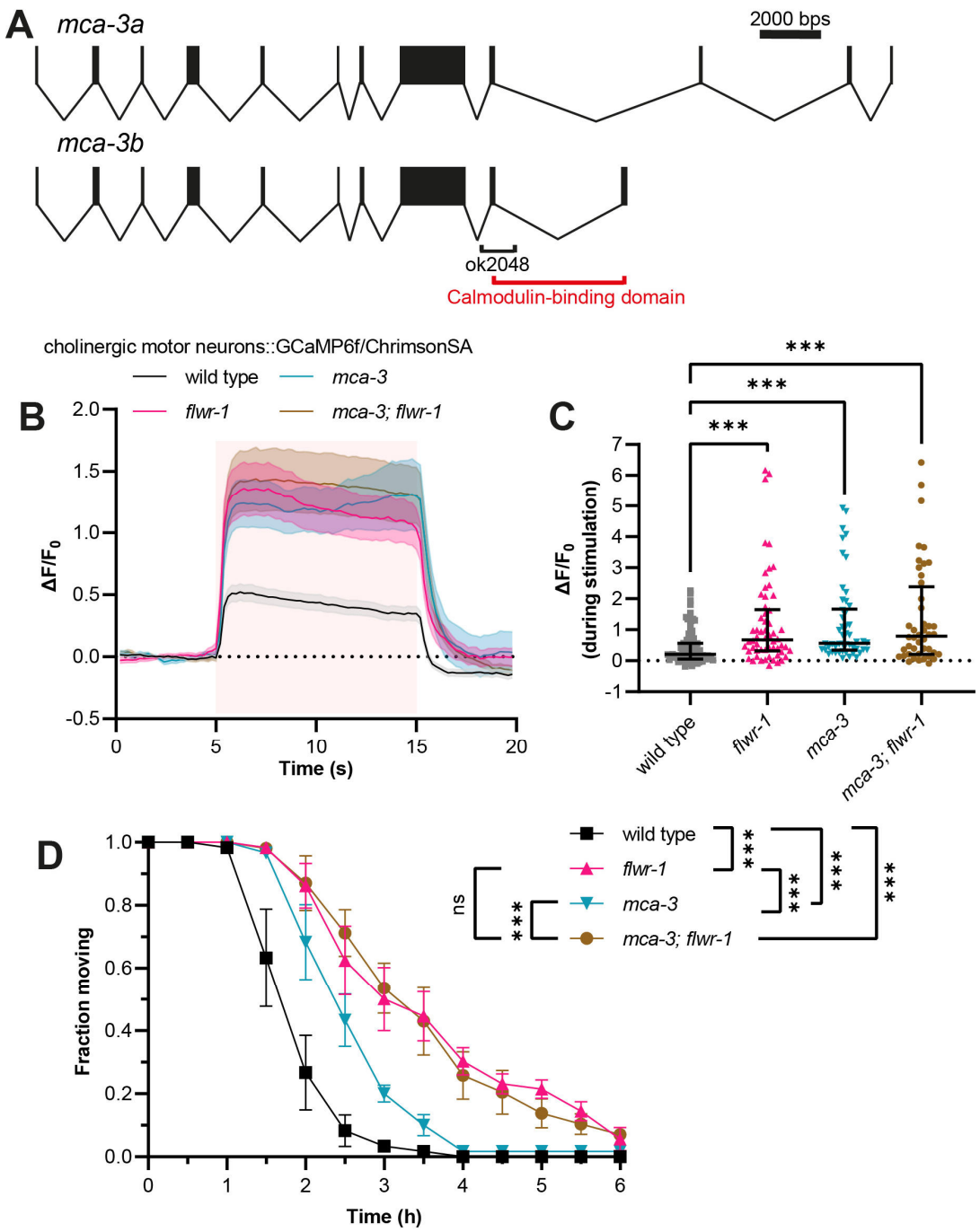

Fig. 7. Increased Ca^{2+} levels in *flwr-1* mutants may be caused by negative regulation of MCA-3.

(A) Schematic representation of the *mca-3* gene locus including exon/intron structure of isoforms *mca-3a* and *mca-3b*. Bars represent exons and connecting lines introns. The size of the *ok2048* deletion as well as the putative calmodulin-binding domain are indicated. **(B)** Mean (± SEM) normalized fluorescence in synaptic puncta of the DNC of animals expressing GCaMP6f and ChrimsonSA in cholinergic motor neurons (*unc-17b* promoter). All animals were supplemented with ATR. A 10 s light pulse (590 nm, 40 µW/mm^2) was applied after 5 s as indicated by the red shade. **(C)** Median (with IQR) normalized fluorescence during stimulation (seconds 6 to 14) as depicted in (B). Each dot indicates a single animal. Kruskal-Wallis test. Only statistically significant differences are depicted. ** $p < 0.01$, *** $p < 0.001$. Number of animals imaged in (B + C): wild type = 83, *flwr-1* = 58, *mca-3* = 50, *mca-3; flwr-1* = 44. Outliers were removed from all datasets as detected by iterative Grubb's method (GraphPad Prism). **(D)** Mean (± SEM) fraction of moving animals after exposure to 1.5 mM aldicarb. Two-way ANOVA with Tukey's correction. ns not significant, *** $p < 0.001$.

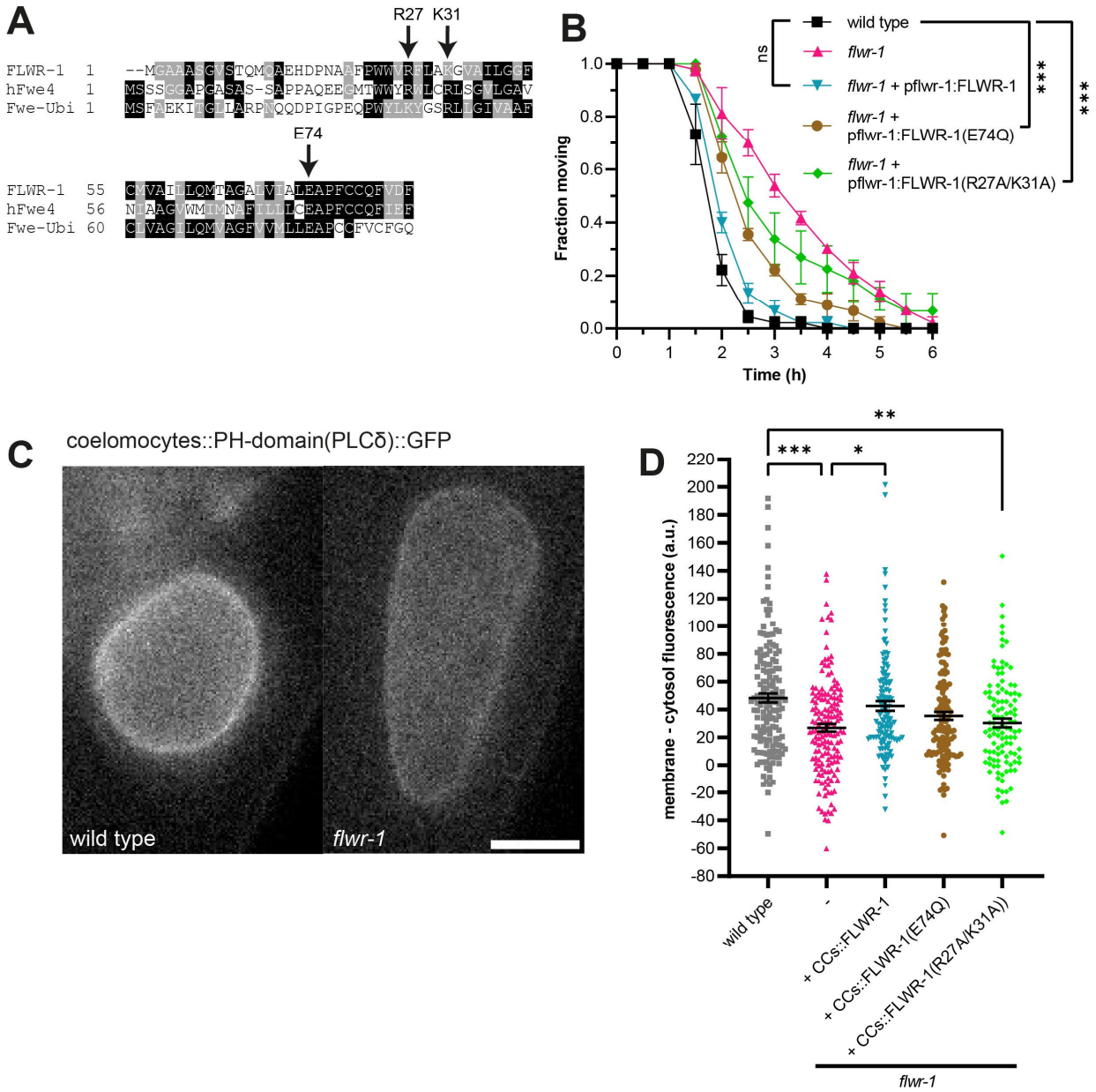

Fig. 8. Basic amino acid residues on the intracellular surface of FLWR-1 may be involved in PI(4,5)P_2 lipid binding.

(**A**) Partial alignment of the amino acid sequences of FLWR-1, hFwe4 (*Homo sapiens*), and Fwe-Ubi/FweA (*Drosophila melanogaster*). Shading depicts evolutionary conservation of amino acid residues (black – identity; grey - homology). (**B**) Mean (± SEM) fraction of moving animals after exposure to 1.5 mM aldicarb. Two-way ANOVA with Tukey's correction. Selected comparisons are depicted. N = 3 biological replicates. *** $p < 0.001$. (**C**) Exemplary images of CCs in wild type and *flwr-1(ok3128)* animals expressing GFP fused to the PH-domain of PLCδin CCs. Scale bar, 10 µm. (**D**) Mean (± SEM) corrected GFP fluorescence. Membrane fluorescence was estimated by measuring the perimeter of CCs and subtracting the fluorescence in the interior of cells. Each dot indicates a single CC. a.u. = arbitrary units of fluorescence intensity. Kruskal-Wallis test. Only statistically significant differences are depicted. * $p < 0.05$, ** $p < 0.01$, *** $p < 0.001$. Number of animals imaged in N = 3 biological replicates: wild type = 27, *flwr-1* = 25.

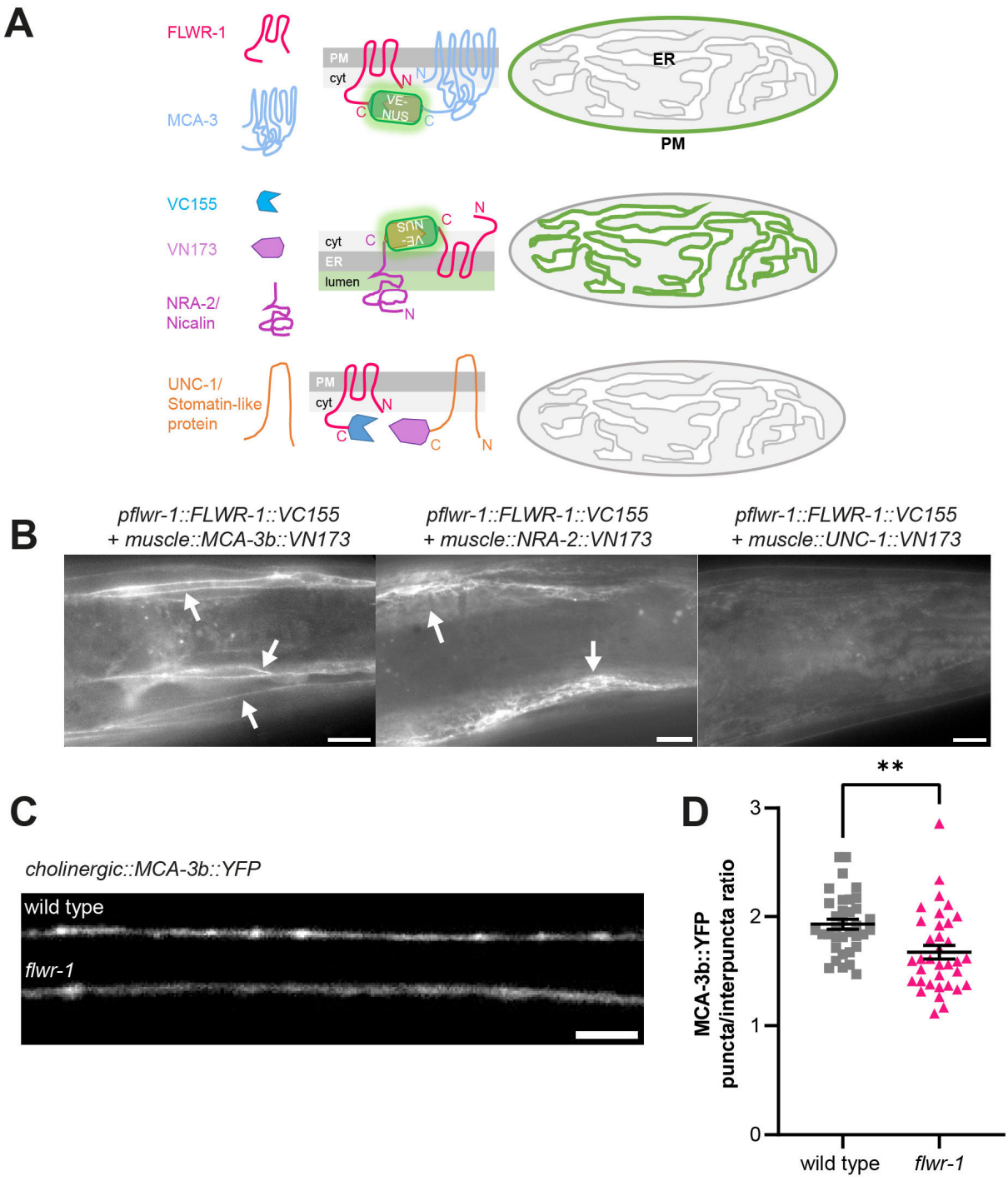

Fig. 9. FLWR-1 is physically close to MCA-3 in the plasma membrane of BWMs and promotes synaptic localization of MCA-3.

(A) Schematic representation of the BiFC assay. **(B)** Representative micrographs of animals expressing FLWR-1 fused to one fragment of mVenus (VN173) and either MCA-3b, NRA-2/Nicalin or UNC-1 stomatin, interacting with gap junctions, respectively, fused to the other fragment of mVenus (VC155). Scale bar, 10 µm. **(C)** Representative micrographs of the DNC of animals expressing MCA-3b::YFP in cholinergic neurons (*unc-17* promoter). Scale bar, 5 µm. **(D, E)** Analysis of MCA-3b::YFP fluorescence (mean ± SEM) along the nerve cord (D) and as the ratio of fluorescence in synaptic puncta over fluorescence in the inter-puncta regions (E). Each dot represents a single animal. Number of animals imaged in N = 3 biological replicates: wild type = 35, *flwr-1* = 35. Unpaired t-test. ** $p < 0.001$.

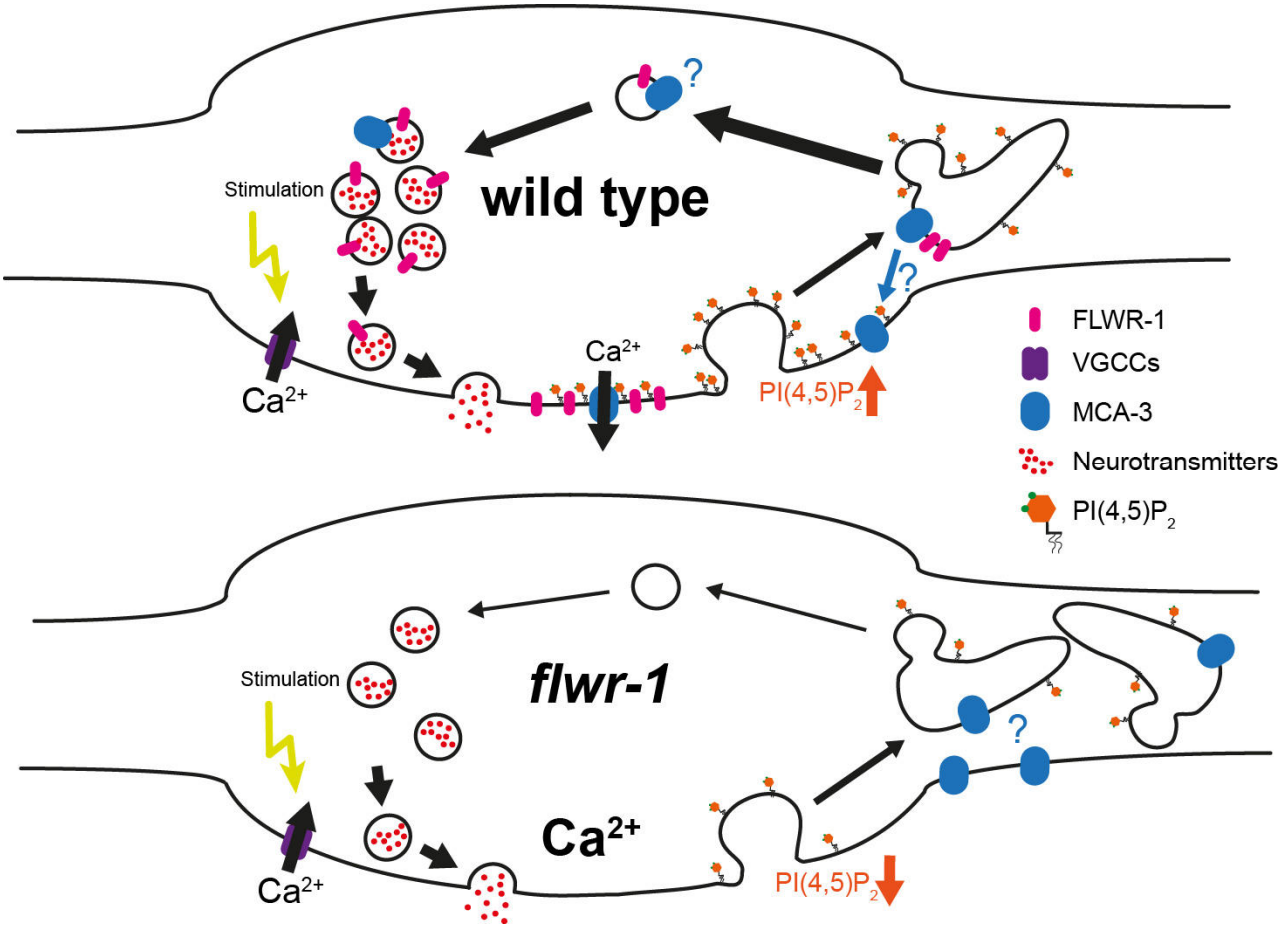

1180

1181 **Fig. 10. Model summarizing findings made in this study.**

1182 For details, see discussion.

1183

1184 **SUPPLEMENTAL MATERIAL**

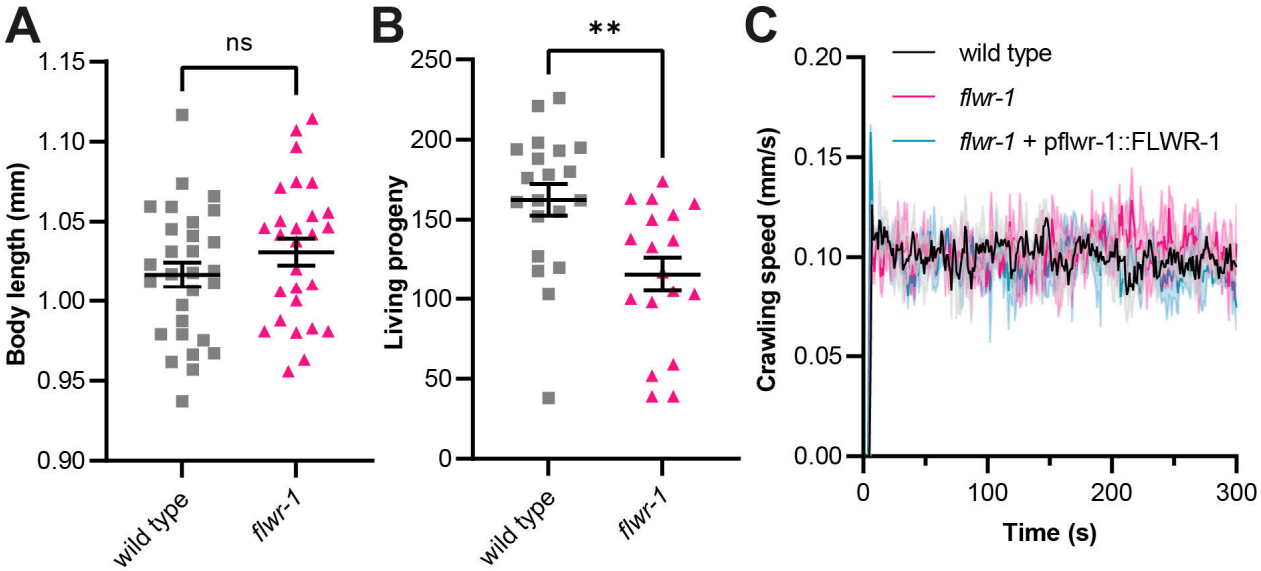

1185

1186 **Figure 1 – Figure supplement 1. Loss of FLWR-1 does not change body length or locomotion speed but reduces the**
1187 **number of living progeny.**

1188 **(A)** Mean (± SEM) body length of wild type and *flwr-1(ok3128)* mutants in mm. Unpaired t-test. ns not significant. Number
1189 of animals accumulated from N = 4 biological replicates: wild type = 29, *flwr-1* = 27. **(B)** Mean (± SEM) number of living
1190 progeny per animal. Unpaired t-test. ** $p < 0.01$. Number of animals accumulated from N = 4 biological replicates: wild
1191 type = 20, *flwr-1* = 18. **(C)** Mean (± SEM) crawling speed. N = 2 biological replicates.

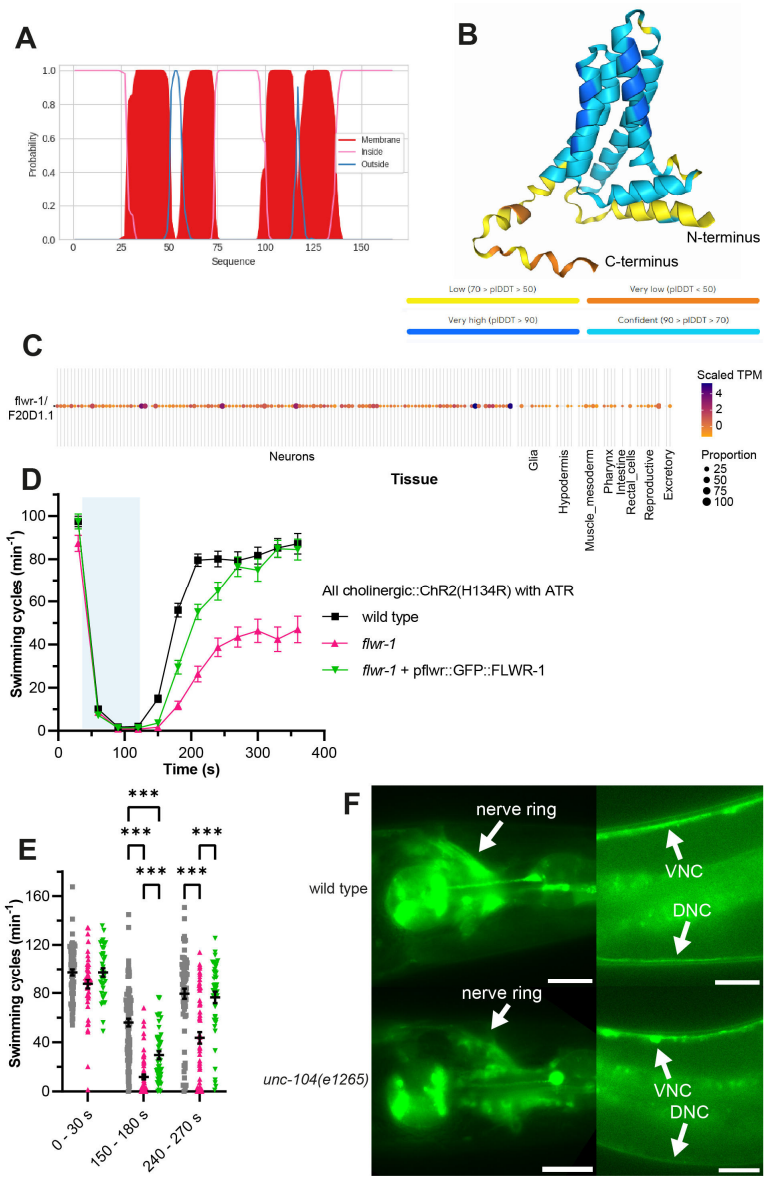

Figure 1 – Figure supplement 2. FLWR-1 is predicted to be a tetraspan transmembrane protein and is transported by UNC-104 kinesin.

(**A**) Graphical representation of the results of DeepTMHMM prediction of membrane orientation of the FLWR-1 protein based on its amino acid sequence. The red shapes indicate the presence of four transmembrane domains. (**B**) Alphafold3 prediction of FLWR-1 protein structure. The coloring represents the calculated predicted local distance difference test (plDDT) as shown below the structure. Higher plDDT values indicate a higher confidence of correct prediction. (**C**) Heatmap plot depicting *flwr-1(F20D1.1)* single-cell RNAseq data generated by the CeNGEN database. Coloring indicates transcripts per million (TPM) per tissue normalized to the average expression as indicated in the legend. The size of the dots represents the percentage of cells of this cell type expressing the gene. (**D**) Mean (± SEM) swimming cycles of animals expressing ChR2(H134R) in cholinergic motor neurons (*unc-17* promoter). All animals were treated with ATR. A 90 s light pulse (470 nm, 1 mW/mm^2) was applied after 30 s as indicated by the blue shade. Number of animals accumulated from N = 2 biological replicates: wild type = 63 – 99, *flwr-1* = 48 – 66, GFP::FLWR-1 rescue = 37 – 52. (**E**) Statistical analysis of swimming speed at different time points as depicted in (D). Mean (± SEM). Each dot represents a single animal. Mixed-effects model analysis with Tukey's correction. Only statistically significant differences are depicted. *** $p < 0.001$. (**F**) Example images depicting GFP::FLWR-1 fluorescence in nerve ring and nerve cords in wild type and *unc-104(e1265)* mutants. Scale bar, 20 µm.

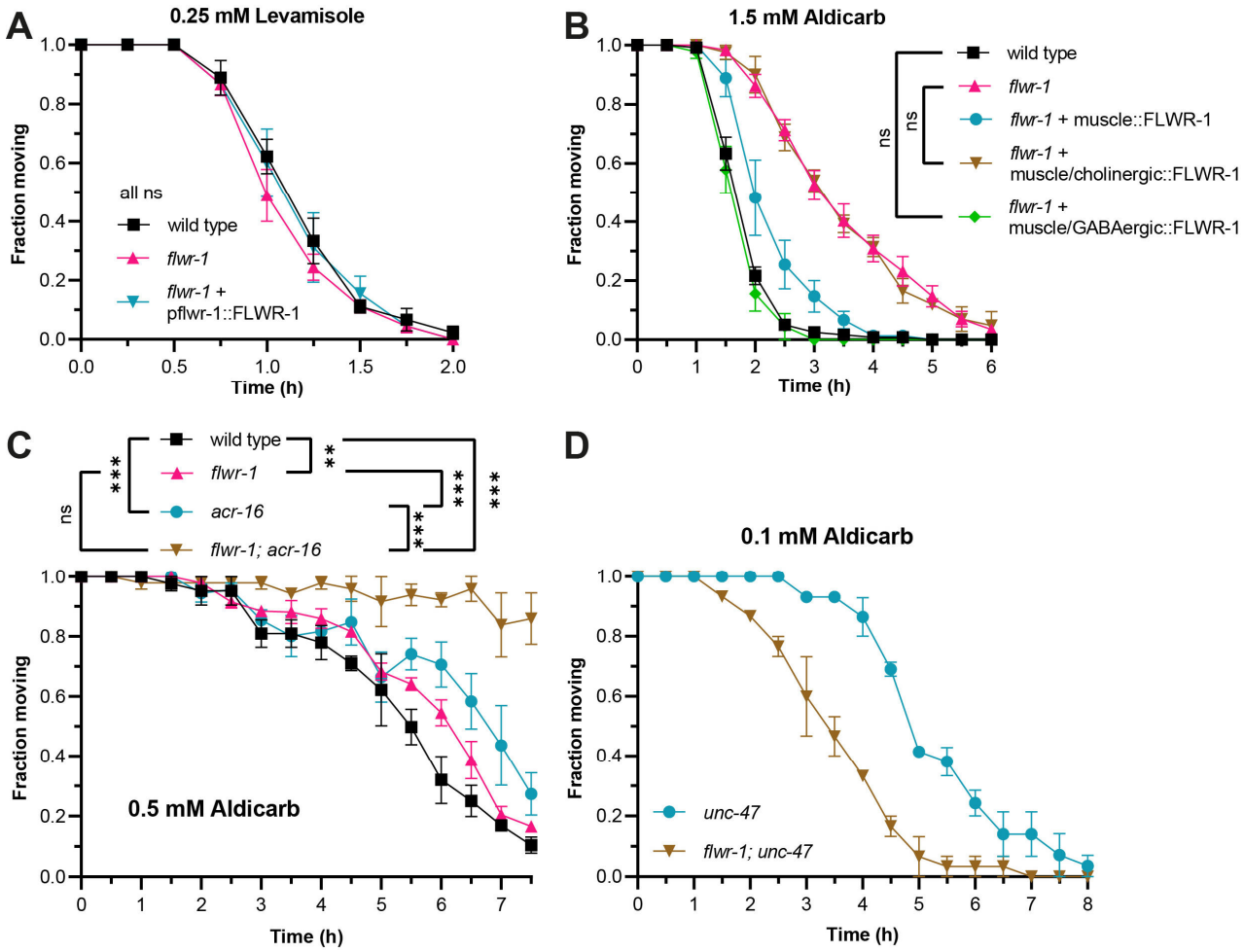

1209

1210 **Figure 1 – Figure supplement 3. FLWR-1 expression in body wall muscle cells partially rescues aldicarb resistance**
1211 **of *flwr-1* mutants, but aldicarb resistance is not affected through AChRs.**

1212 (**A**) Mean (± SEM) fraction of moving animals after exposure to 0.25 mM levamisole. N = 3 biological replicates. Two-
1213 way ANOVAs with Tukey's correction. No significant differences were found. **(B)** Mean (± SEM) fraction of moving
1214 animals after exposure to 1.5 mM aldicarb. FLWR-1 is optionally expressed in BWMs (*pmyo-3*) only or combined with
1215 expression in cholinergic (*unc-17p*) or GABAergic (*unc-47p*) neurons in a *flwr-1(ok3128)* mutant background. N = 3 - 8
1216 biological replicates. Two-way ANOVAs with Tukey's correction. Only non-significant differences are depicted. For all
1217 other comparisons $p < 0.001$. (**C**) Mean (± SEM) fraction of moving animals after exposure to 0.5 mM aldicarb, compared
1218 in wild type, *flwr-1(ok3128)*, *acr-16(ok789)* and *flwr-1; acr-16* double mutants. N = 3 biological replicates. Two-way
1219 ANOVAs with Tukey's correction. **(D)** Loss of GABAergic transmission conveys aldicarb hypersensitivity in *flwr-1*
1220 mutants. Mean (± SEM) fraction of moving animals after exposure to 0.1 mM aldicarb. N = 3 biological replicates.

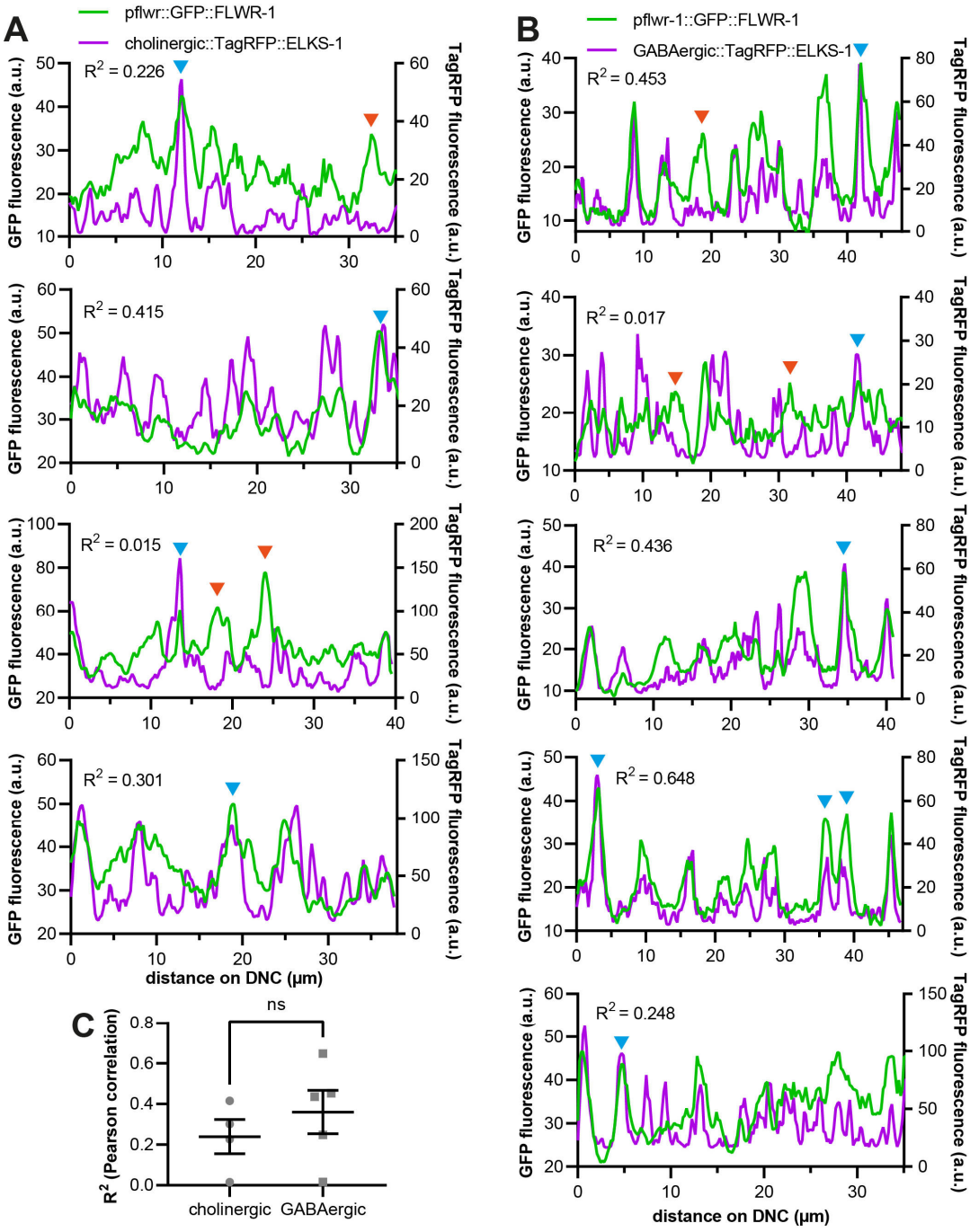

Figure 3 – Figure supplement 1. FLWR-1 localizes to cholinergic and GABAergic active zones.

(A) Line scan analysis of colocalization of GFP::FLWR-1 and TagRFP::ELKS-1 along the DNC as represented in the same order in **Fig. 3B**. R^2 as determined by Pearson correlation. a.u. = arbitrary units of fluorescence intensity. **(B)** Line scan analysis of colocalization of GFP::FLWR-1 and TagRFP::ELKS-1 along the DNC as represented in the micrographs in the same order in **Fig. 3C**. R^2 as determined by Pearson correlation. a.u. = arbitrary units of fluorescence intensity. **(A + B)** Examples for fluorescent puncta which contain either both, FLWR-1 and ELKS-1 (blue arrowheads), or only FLWR-1 (red arrowheads) are indicated. The same puncta are indicated in the respective micrographs in Fig. 3B + C. **(C)** Comparison of Pearson correlation coefficients of line scans along DNCs represented in **Fig. 3**. Mean (± SEM). Unpaired t-test.

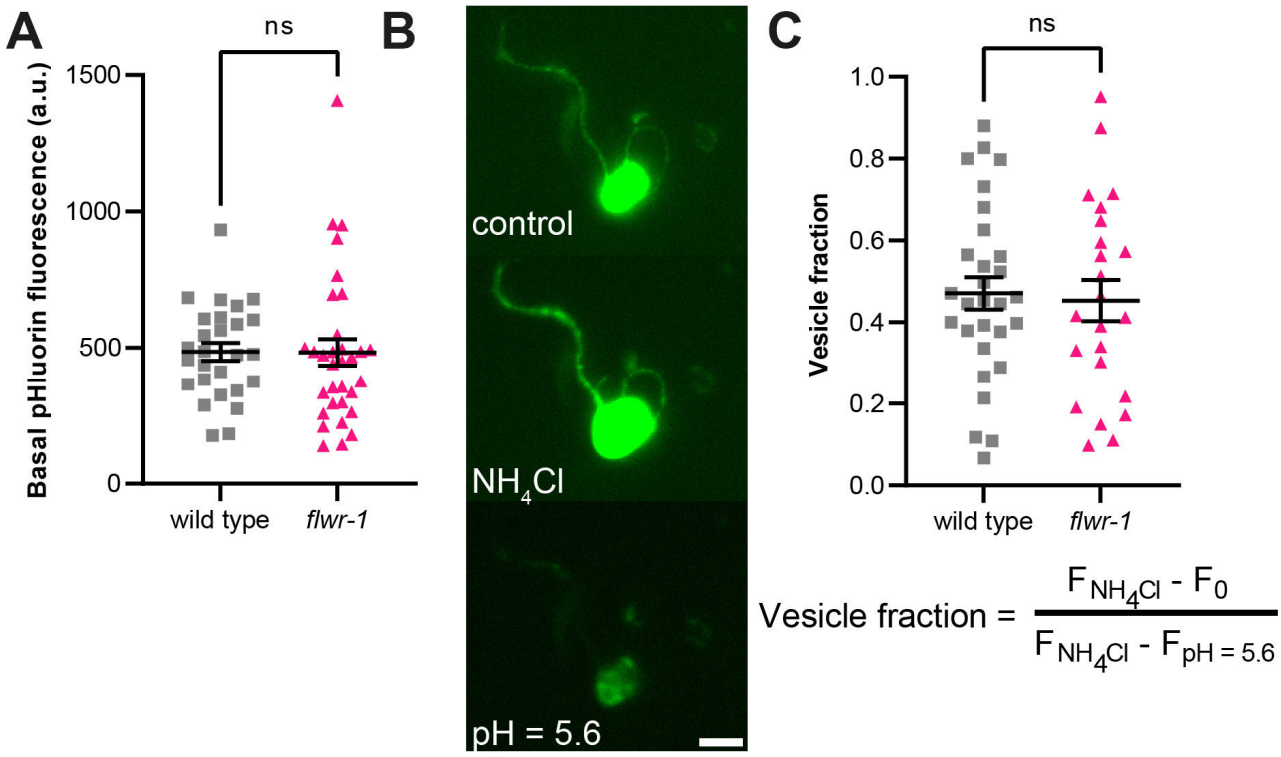

1230

1231 **Figure 4 – Figure supplement 1. Basal SNG-1::pHluorin fluorescence and cell surface fraction are unchanged in**
1232 ***flwr-1* mutants.**

1233 **(A)** Mean (± SEM) pHluorin fluorescence before stimulation as depicted in Fig. 5. Number of animals imaged in N = 5
1234 biological replicates: wild type = 27, *flwr-1* = 32. Unpaired t-test. ns not significant $p > 0.05$. **(B)** Representative images of
1235 a primary neuronal cell expressing SNG-1::pHluorin when exposed to different buffers as indicated. Scale bar, 5 µm. **(C)**
1236 Number of cells imaged in N = 2 biological replicates: wild type = 29, *flwr-1* = 23. Unpaired t-test. ns not significant $p >$
1237 0.05.

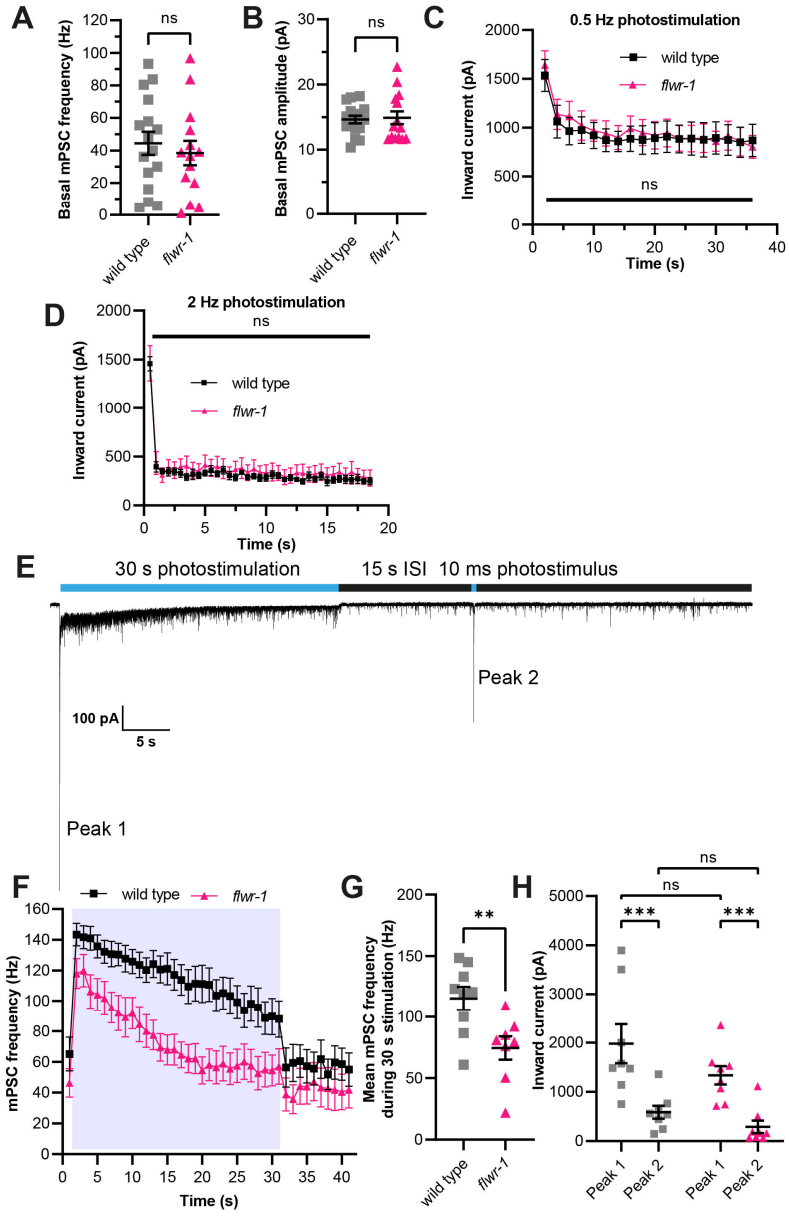

Figure 5 – Figure supplement 1. *flwr-1* mutants show defecting cholinergic neurotransmission only during continuous stimulation.

(A, B) Mean (± SEM) mPSC frequency and amplitude, respectively, before stimulation. Unpaired t-test. ns not significant. Number of animals: wild type = 16, *flwr-1* = 14. **(C)** Mean (± SEM) inward currents of BWMs recordings induced by 10 ms light pulses (470 nm, 8 mW/mm^2) applied every 2 s (0.5 Hz). Two-way ANOVA with Šidák's correction for multiple comparisons. ns not significant. Number of animals: wild type = 9, *flwr-1* = 8. **(D)** As in (C), but 2Hz stimulation. ns not significant. Number of animals: wild type = 7, *flwr-1* = 7. **(E)** Representative voltage-clamp recording of currents detected in BWMs. This wild type animal expresses ChR2(H134R) in cholinergic motor neurons (*unc-17* promoter) and has been treated with ATR. A 30 s light stimulus (470 nm, 8 mW/mm^2) as well as a 10 ms pulse after a 15 s inter-stimulus interval (ISI) were applied as indicated by blue bars. **(F)** Mean (± SEM) mPSC frequency in BWMs of animals expressing ChR2(H134R) in cholinergic motor neurons (*unc-17* promoter). All animals have been treated with ATR. A 30 s light pulse (470 nm, 8 mW/mm^2) was applied as indicated by blue shade. **(G)** Mean (± SEM) mPSC frequency during 30 s stimulation. Unpaired t-test. ** $p < 0.01$. **(H)** Analysis of the amplitude of the first peak during 30 s photostimulation and the second peak after 15 s ISI as indicated in (E). Two-way ANOVA with Tukey's correction for multiple comparisons. ns not significant, *** $p < 0.001$. (F - H) Number of animals: wild type = 9, *flwr-1* = 8.

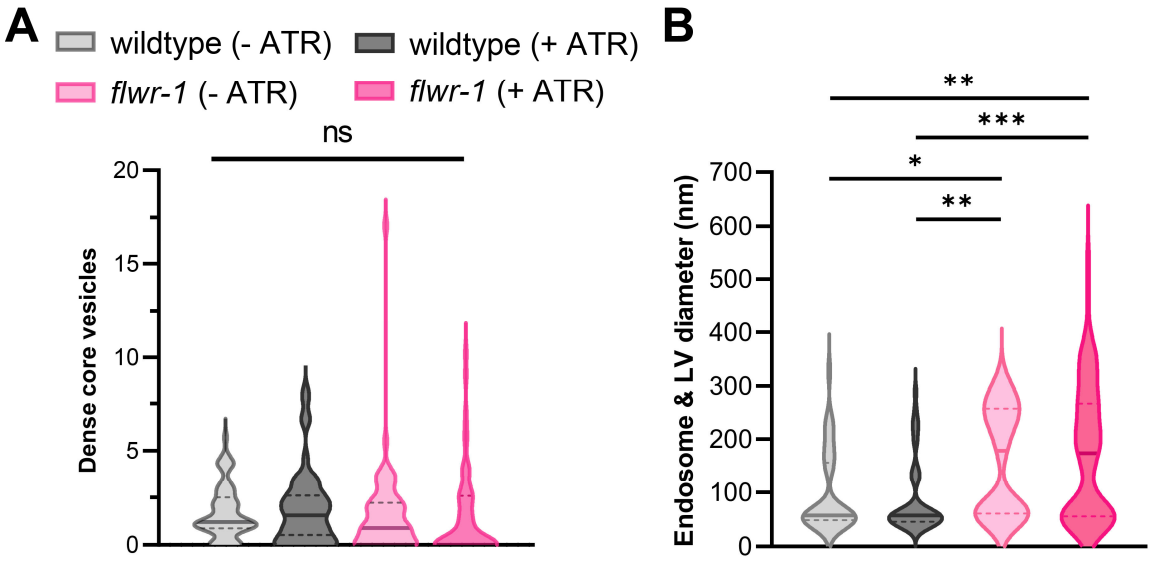

Figure 6 – Figure supplement 1. *flwr-1* mutants have a normal numbers of dense core vesicles before and after stimulation, but increased size endosomes and LVs.

(A) Violin plot depicting the number of dense core vesicles counted per synaptic profile. **(B)** Diameters of endosomes and large vesicles, combined. Bold line represents the median and the dashed lines the IQR. Kruskal-Wallis test. ns not significant. Number of synaptic profiles imaged: wild type (-ATR) = 56, wild type (-ATR) = 51, *flwr-1* (-ATR) = 55, *flwr-1* (+ATR) = 59.

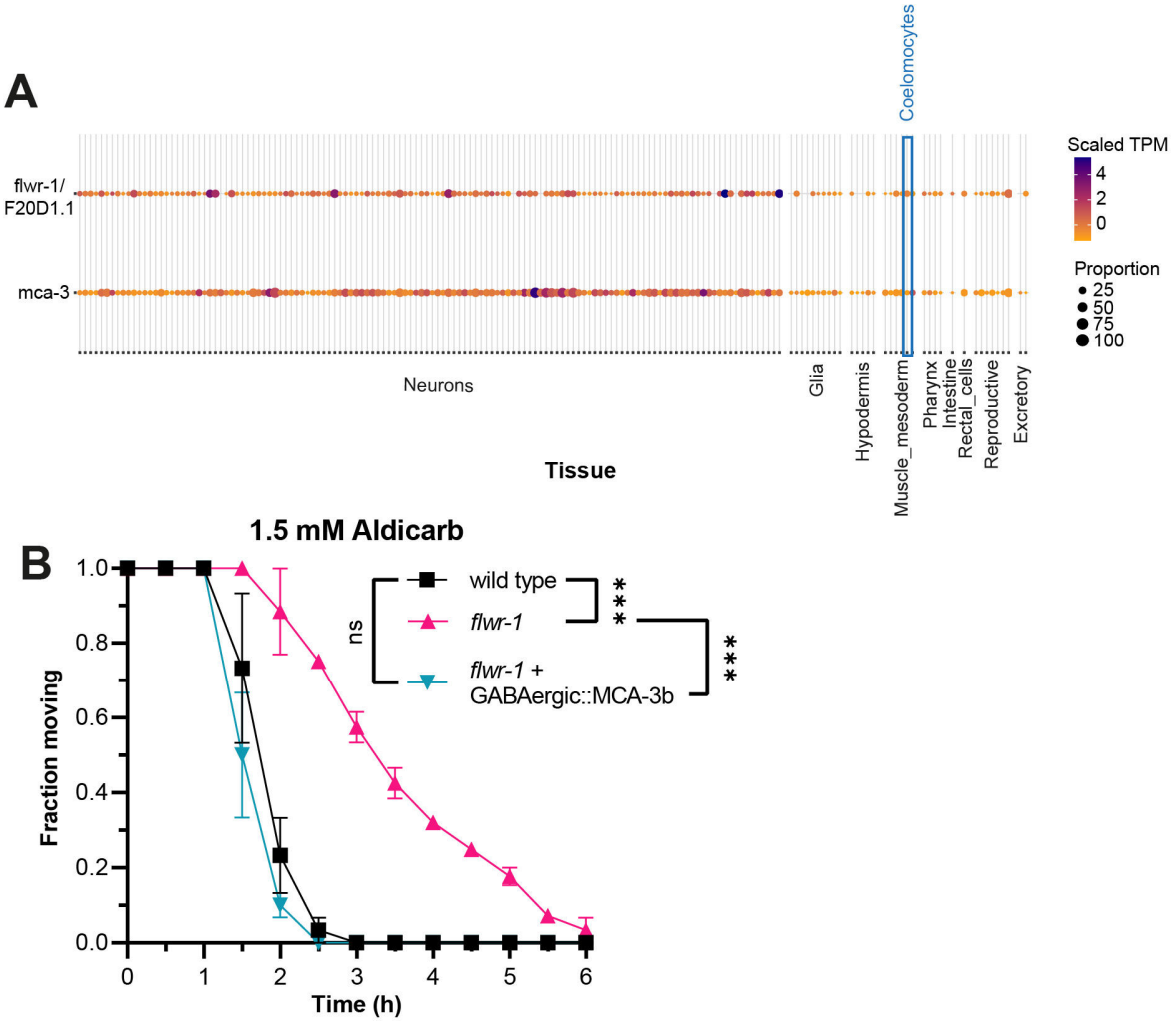

Figure 7 – Figure supplement 1. Comparison of *flwr-1* and *mca-3* expression by single-cell RNAseq data.

(A) Heatmap plot depicting *flwr-1(F20D1.1)* and *mca-3* single-cell RNAseq data generated by the CeNGEN database (https://cengen.shinyapps.io/CengenApp/). Coloring indicates transcripts per million (TPM) per tissue normalized to the average expression as indicated in the legend. The size of the dots represents the percentage of cells of this cell type expressing the gene. Coelomocyte data is highlighted by the blue box. **(B)** Mean (± SEM) fraction of moving animals after exposure to 1.5 mM aldicarb. MCA-3b is expressed in GABAergic neurons of *flwr-1(ok3128)* mutant animals (*unc-47* promoter). Two-way ANOVA with Tukey's correction. N = 3 biological replicates. ns not significant $p > 0.05$, *** $p < 0.001$.

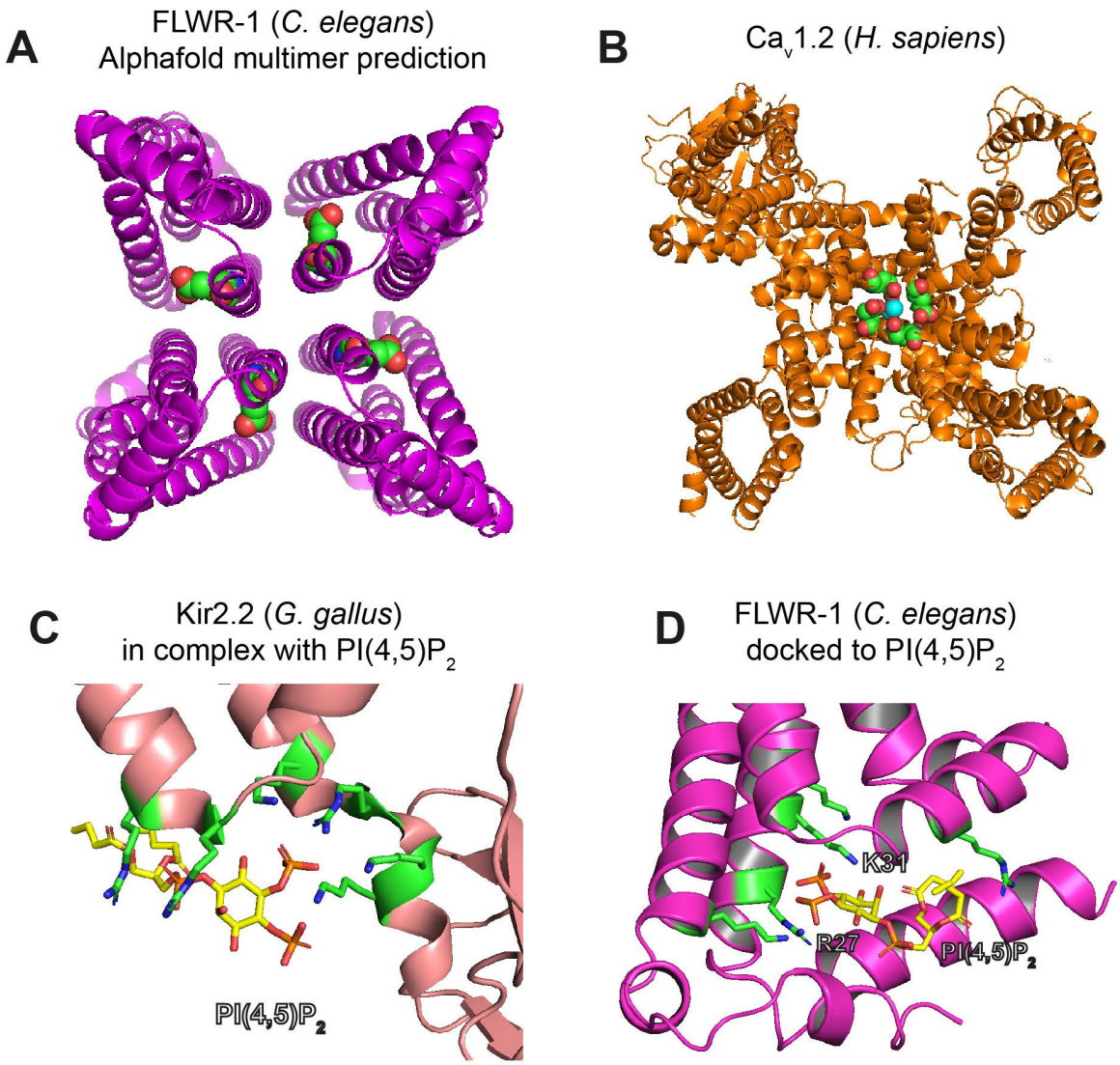

1270

1271 **Figure 8 – Figure supplement 1. Structural analysis of important amino acid residues in FLWR-1 and other proteins.**

1272 **(A)** Top view of an Alphafold3 prediction of a tetrameric FLWR-1 structure. Glutamate 74 is indicated as colored spheres
1273 in each monomer. **(B)** Cryo-EM structure of the human L-type voltage-gated calcium channel $Ca_v1.2$ (PDB: 8EOG) (Chen
1274 et al., 2023). Glutamate residues in the central pore are indicated as spheres. Ca^{2+} ions within the pore are depicted as
1275 turquoise spheres. **(C)** X-Ray structure of the Kir2.2 potassium channel in a complex with $PI(4,5)P_2$ (PDB: 3SPI) (Hansen
1276 et al., 2011). Basic amino acid residues in the proximity of $PI(4,5)P_2$ are depicted as sticks. **(D)** $PI(4,5)P_2$ was docked to the
1277 Alphafold3 structure of FLWR-1 using AutoDock Vina (Eberhardt et al., 2021). Basic amino acid residues in the proximity
1278 of $PI(4,5)P_2$ are depicted as sticks. Arginine 27 and lysine 31 are indicated.

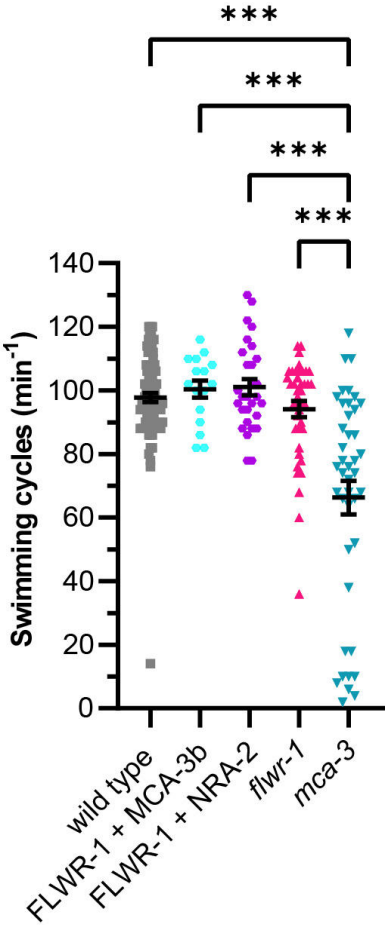

1279

1280 **Figure 9 – Figure supplement 1. Expression of FLWR-1 and MCA-3b for BiFC does not affect locomotion behavior:**
1281 Mean (± SEM) swimming cycles of animals analyzed by BiFC as depicted in Fig. 8B. N2 wild type animals were used as
1282 a control strain, as well as *flwr-1(ok3128)* and *mca-3(ok2048)* mutants. Number of animals accumulated from N = 4 (wild
1283 type) or N = 2 (all other strains) biological replicates: wild type = 90, FLWR-1/MCA-3b = 16, FLWR-1/NRA-2 = 29, *flwr-*
1284 *1* = 40, *mca-3* = 42 . One-way ANOVA with Tukey's correction. ns not significant $p > 0.05$, *** $p < 0.001$.

1285

1286

1287 ## Additional Files

1288 **Table S1: Plasmids used in this study.**

1289 **Table S2: Strains used in this study.**

1290 **Table S3: CeNGEN expression data of *flwr-1/F20D1.1* and *mca-3***

1291 Single-cell RNAseq data as described in Taylor et al. (2021). The threshold was set to "All Cells Unfiltered". Cell types
1292 were sorted alphabetically. Where CeNGEN did not produce any results, cells were left blank.

1293 **Movie S1.**
1294 Time series of a particle containing GFP::FLWR-1 and mCherry::SNB-1 travelling along commissures. Scale bar, 2 µm.